Analytical Exponential-6 Equation of State Based on Monte Carlo Simulations

by Peter Hallstadius

LUND
UNIVERSITY

Thesis for the degree of Master of Science
Thesis advisor: Prof. Xue-Song Bai

To be presented, with the permission of the Faculty of Engineering of Lund University, for public criticism on the online meeting at the Department of Energy Sciences on Friday, the 26th of February 2021 at 13:15.

This degree project for the degree of Master of Science in Engineering has been conducted at the Division of Fluid Mechanics, Department of Energy Sciences, Faculty of Engineering, Lund University.

Supervisor at the Division of Fluid Mechanics was Professor Xue-Song Bai.

Examiner at Lund University was Professor Johan Revstedt.

Department of Energy Sciences
Faculty of Engineering
Lund University

ISSN: <0282-1990>
LUTMDN/TMHP-21/5468-SE

Typeset in LaTeX
Lund 2021

Abstract

The exponential-6 (exp-6) potential is an intermolecular pair potential that is widely used to model fluids at high densities. The path from molecular interaction to equation of state (EOS) for a gas is not straightforward however. Monte Carlo methods and molecular dynamics give accurate results but are too slow for demanding applications like detonation modelling or numerical simulations of reactive flows. In this thesis, I propose a new equation of state in the form of an analytical expression for the excess Helmholtz free energy of an exp-6 fluid. All other thermodynamic properties are obtained as derivatives of this expression and gas mixtures are treated as an effective simple fluid. The equation of state is based on extensive Monte Carlo simulations and therefore combines the excellent accuracy of the simulations with the numerical efficiency of a polynomial expression. The average relative error in compressibility factor and internal energy is 0.14% and 0.25% respectively, which is a significant improvement over statistical mechanical theories. The number of polynomial coefficients was also significantly reduced compared to previous equations of state, through the use of a new variable transformation. The EOS was implemented into a thermochemical code in order to optimise gas parameters and evaluate its performance on pure gas data, shock compression and detonation properties. Gas densities were typically predicted to within 1.5% at pressures below 1 GPa and temperatures above 300 K. Calculated shock Hugoniots showed excellent agreement with experimental values up to 150 GPa and 15 000 K, and the detonation performance was accurately predicted for a number of different types explosives.

Acknowledgments

I would like to thank my supervisor Professor Xue-Song Bai for his everlasting support and valuable feedback throughout my entire project. He also connected me with two of his colleagues at the Department of Energy Sciences: Michael Bertsch, who took time to teach me how to use the supercomputer, and Robert-Zoltan Szasz, whose insights led to a vastly improved method for data processing.

I must also express my gratitude to my friends Erik Blåe and Carolina Rudervall for always listening to my problems, mistakes and breakthroughs.

The simulations have been performed on resources provided by the Swedish National Infrastructure for Computing (SNIC) at NSC.

Contents

List of Figures

List of Tables

Nomenclature

Greek Letters

α	Stiffness of repulsion	[-]
α_ℓ	Transformed stiffness of repulsion	[-]
β	Coldness; $1/(k_B\,T)$	[J^{-1}]
ε	Potential well depth	[J]
μ	Chemical potential	[$\mathrm{J\,mol}^{-1}$]
μ^*	Dimensionless excess chemical potential	[-]
Φ	Trivariate Chebyshev polynomial which defines the free energy	[-]
ρ	Density	[$\mathrm{kg\,m}^{-3}$]
ρ^*	Dimensionless particle density	[-]
τ	Transformed reduced temperature	[-]
$\tilde{\alpha}$	Scaled transformed stiffness of repulsion	[-]
$\tilde{\tau}$	Scaled transformed temperature	[-]
$\tilde{\zeta}$	Scaled transformed density	[-]
ζ	Transformed reduced density	[-]

Roman Letters

A	Helmholtz free energy	[J]
c	Speed of sound	[$\mathrm{m\,s}^{-1}$]
c_V	Specific heat capacity at constant volume	[$\mathrm{J\,kg}^{-1}\,\mathrm{K}^{-1}$]

F	Dimensionless excess Helmholtz free energy	[-]
k_B	Boltzmann constant	[J K^{-1}]
N	Number of particles	[-]
n	Amount of gas	[mol]
p	Pressure	[Pa]
R	Ideal gas constant	[J mol^{-1} K^{-1}]
r_m	Distance to the intermolecular potential minimum	[Å]
T	Temperature	[K]
T^*	Dimensionless temperature	[-]
U	Internal energy	[J]
U^*	Dimensionless excess internal energy	[-]
V	Volume	[m^3]
Z	Compressibility factor	[-]

Abbreviations

BKW Becker-Kistiakowsky-Wilson

EOS Equation of state

HMSA Hypernetted-mean spherical approximation

JCZ Jacobs-Cowperthwaite-Zwisler

KLRR Kang-Lee-Ree-Ree perturbation theory

MC Monte Carlo

MCRSR Mansoori-Canfield-Rasaiah-Stell/Ross hard-sphere variational theory

MD Molecular dynamics

PRNG Pseudorandom number generator

Chapter 1.

Introduction

1.1. Background

As early as 1662, Robert Boyle showed experimentally that the pressure of air is inversely proportional to its volume [1]. In mathematical terms, this may be described as

$$pV = \text{constant} \, . \tag{1.1}$$

Over the years, the quantity of gas and its temperature dependence was included and the equation developed into the well-known ideal gas law,

$$pV = nRT \, . \tag{1.2}$$

The right hand side contains the number of moles of gas n, the ideal gas constant R, and the absolute temperature T. From a theoretical point of view, the ideal gas law is justified by assuming pointlike gas particles and elastic collisions.

There are however many applications where intermolecular forces and the finite sizes of the gas molecules cannot safely be ignored. This includes simulations of high-pressure reactive flows in internal combustion engines and gas turbines, and even more non-ideal conditions are reached in detonations and strong shock waves. Common for all these applications is the need to accurately model a mixture of many different gases. Furthermore, chemical equilibrium calculations require repeated evaluations of the gas properties [2], so an equation of state used for this purpose should be numerically efficient and accurate over a wide range of conditions.

There are however no simple equations or analytic solutions when the intermolecular forces and molecular sizes are taken into account. Many approximations and corrections to the ideal gas law have been proposed, but to get arbitrarily accurate results, statistical methods are necessary. In 1953, Metropolis et al. published a new Monte Carlo (MC) algorithm for statistical mechanical simulations of systems composed of individual molecules [3]. Using the first electronic computers available for research, they simulated a two-dimensional hard-sphere fluid. Three years later, the first molecular dynamics

(MD) simulation followed. Both methods are exact in the sense that they perfectly reproduce the macroscopic properties of a fluid, given a sufficiently accurate model for the intermolecular interactions in that fluid [4].

However, MC and MD simulations were, and are, extremely computationally expensive and simulations of reactive gas mixtures were far beyond the capabilities of existing computers. Early calculations of high-pressure mixtures instead used a much more empirical approach. The Becker-Kistiakowsky-Wilson equation of state (BKW EOS) was implemented and calibrated by Mader in the early 1960s and used to calculate the properties and chemical equilibrium compositions in detonations [5].

The BKW EOS is given below [2]:

$$\begin{aligned} pV &= nRT(1 + xe^{\beta x}) \\ x &= \frac{\kappa k}{V(T+\theta)^{\alpha}} \,, \end{aligned} \tag{1.3}$$

where α, β, κ and θ are empirical constants. k is the mean covolume of the gas mixture, essentially the average molecular volume. While the form of the equation of state has some statistical mechanical motivation [6], the coefficients are empirical and numerous sets of coefficients have been proposed [6]–[9]. These have been calibrated from various experimental detonation data and generally produce much worse predictions for cases not included in the calibrations.

In 1976, Cowperthwaite and Zwisler published a more theoretical equation of state for hot, high-pressure detonation products: the Jacobs-Cowperthwaite-Zwisler (JCZ3) EOS [10]. The EOS models the behaviour of a simple fluid interacting with the exponential-6 (exp-6) intermolecular potential. The result is generalised to any real gas mixture by averaging the potential parameters of each gas. The exponential-6 potential and treatment of mixtures are discussed in more detail in the theory section.

The JCZ3 EOS has a somewhat unusual form with the pressure split into two analytical functions: $p_0(V)$, which is the pressure in a crystalline lattice at 0 K, and $G(V,T)$ which contains the thermal contributions in the gas.

$$p = p_0(V) + G(V,T)\frac{nRT}{V} \tag{1.4}$$

Several parameterisations of gas potential parameters have been performed over the years. Early ones used shock compression experiments (so called shock Hugoniots) of common fluids like water, nitrogen and carbon dioxide to determine the radii and potential well depths of the gases. The parameters were then adjusted to better fit experimental detonation velocities [11]. The stiffness of repulsion at short ranges was set to the same constant value for all gases. More recent work [12] has shown that detonation properties can be adequately predicted without calibrating the EOS to detonation properties, however, "potential compensation" was required since all

molecules are not equally repulsive in reality. The apparent stiffness of a molecule can be increased by decreasing its radius and increasing the potential well depth, in order to properly fit shock experiments at high temperature and pressure. Since the potential well depth is closely tied to the critical temperature of fluids [13], this method is less accurate when individual gases are considered. Carbon tetrafluoride for example has been modeled as a very stiff molecule by other authors [14] and the potential compensation in the JCZS3 product library overestimates the critical temperature of CF_4 by a factor of twenty [12], [15].

The advent of new theories and greater available computer power in the 1980s allowed Ree to to take a different, more theoretical approach to the problem. He used a fluid theory based on statistical mechanics, Ross's modification of the Mansoori-Canfield-Rasaiah-Stell hard-sphere variational theory (MCRSR) to numerically calculate the properties of an exp-6 gas [16]. It was combined with a new improved mixing rule for gases which allowed the use of different stiffnesses and implemented into the thermochemical code CHEQ [17]. He achieved good agreement with experimental detonation measurements without fitting EOS parameters to such data, unlike BKW and JCZ3.

The computational effort required to repeatedly solve MCRSR numerically during equilibrium calculations was still enormous, so simulations without supercomputers were practically impossible. Brown solved this problem in 1986 by creating an analytical representation of the WCA/Ree hard-sphere perturbation theory, achieving a hundredfold speedup [18]. The two key features of his work was to fit a Chebyshev polynomial to the excess free energy F of the gas, and the use of transformed variables. The gas law is

$$pV = nRT\left(1 + \rho\left(\frac{\partial F}{\partial \rho}\right)_T\right) , \tag{1.5}$$

where ρ is the density of the gas. F is not a very well-behaved function in terms of the temperature, density, and stiffness coefficient of the gas mixture. Brown therefore proposed a transformation to $F(x, y, z)$ which gave the polynomial 10 to 40 times better accuracy. The variables x, y and z are defined as

$$\begin{aligned} x &= 1/\alpha_\beta \\ y &= 1/T_\alpha \\ z &= \rho^* \left(\alpha_\beta/\alpha\right)^3 , \end{aligned} \tag{1.6}$$

where ρ^* is the reduced particle density, α is the stiffness coefficient and α_β and T_α are given by:

$$\begin{aligned} \alpha_\beta &= \alpha - \log T^* - \log\left(\frac{\alpha - 6}{6}\right) \\ T_\alpha &= T^* \left(\alpha_\beta/\alpha\right)^6 (1 - 6/\alpha) . \end{aligned} \tag{1.7}$$

T^* is the reduced temperature. This approach gave excellent representation of the statistical mechanical theory and close agreement with Monte Carlo simulations using

only 64 Chebyshev polynomial coefficients, within a limited temperature and density range. He called this the THEOSTAR equation of state.

Since then, Brown's transformation has been used several times with more accurate statistical mechanical theories. Fried and Howard used Zerah and Hansen's hypernetted-mean spherical approximation (HMSA), an integral equation theory, to fit an analytical EOS (HMSA/C) over a much larger range of conditions [19]. The region of interest was split into 20 domains and a Chebyshev polynomial was interpolated in each domain. They then used 57 Monte Carlo simulations to calculate a correction term, resulting in the very accurate HMSA/MC. This EOS is used in the thermochemical code Cheetah.

Victorov et al. improved the Kang-Lee-Ree-Ree perturbation theory (KLRR) [20] and used it to generate the thermodynamic data. Similarly to the approach of Fried and Howard, they split the region of interest into smaller domains and interpolated around 200 Chebyshev polynomials [21], again using Brown's transformation [20]. The analytical EOS is implemented in the TDS code.

Suceska et al. followed Brown's original approach with a single interpolation domain to create the equation of state used in the EXPLO5 code [21]. It is valid for a somewhat smaller range of thermodynamic states but uses much fewer Chebyshev coefficients. The KLRR theory was used to generate the thermodynamic data. Other noteworthy thermochemical codes are Carte [22], which uses MCRSR and improved KLRR; Tiger [10], which uses the newly reparameterised JCZ [12]; and Jaguar [23], which also uses JCZ.

Even though Brown's transformation has been used very successfully over the years, there is still room for improvement. The main issue is that the region of interest in xy-coordinates is boot-shaped rather than a rectangle, as shown in figure 1.1.

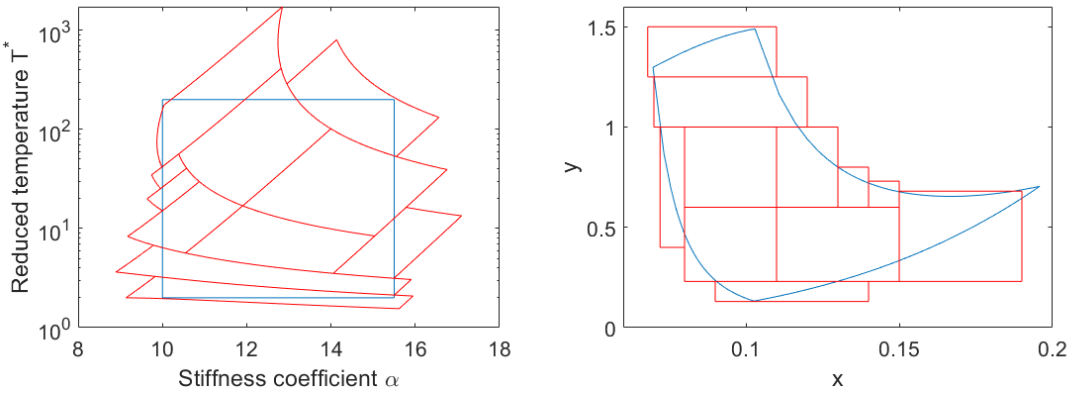

Figure 1.1. The region of interest (blue) and domains (red) in HMSA/C by Fried and Howard [19], shown in both the natural αT^*-system and the transformed xy-system.

Therefore it must be much bigger to encompass the rectangular α, T^*-region, and as much as half of the points used during the polynomial interpolation could lie outside the region of interest [18]. For very large temperature ranges, the transformation completely fails in the single-domain case. Splitting the region into several smaller domains mediates the problem somewhat, however one of Fried and Howard's domains still reaches eight times the intended upper temperature limit.

The $\rho^* \rightarrow z$ transformation on the other hand normalises the upper density boundary fairly well. Brown noted that $z = 1$ approximates the freezing density of a hard-sphere fluid regardless of temperature [18]. However, Suceska showed that z can be as high as 1.8 in certain shock phenomena [21], which is far above the freezing density of an exp-6 fluid at low temperatures [24]. This can again be mediated by the use of several domains, but it comes at a cost. There is on one hand the problem of domain boundaries, since the excess free energy function and its derivatives must be continuous, and on the other hand is the sheer number of coefficients required when each domain has its own polynomial. Victorov and Gubin used around 40000 coefficients [21] which is far more than what should be required. A new transformation, with a better balance between well-behaved free energy function and domain simplicity would be highly desirable.

The majority of the error in these equations of state can be attributed to the statistical mechanical theories themselves. They have been used to generate thermodynamic data for the analytical fit simply because they are much faster than Monte Carlo methods and molecular dynamics. Thousands or tens of thousands of data points are required for polynomial interpolation, and to compute these with sufficient accuracy requires so much computational power that it has been impossible — until recently. Statistical mechanical theories still have the advantage of generating a smooth function, while MC and MD are stochastic by nature. With sufficient smoothing however, it should be perfectly possible to generate an equation of state with Monte Carlo calculations only.

1.2. Objective

The objectives of this project are threefold:

- **To create a new equation of state directly from Monte Carlo simulations.** It should achieve better accuracy than current equations of state based on statistical mechanical theories, and only use a single domain.
- **To implement the equation of state into a thermochemical code.**
- **To evaluate its performance on experimental data.** This project focuses on the thermodynamic properties of pure gases, shock compression- and detonation modelling.

1.3. Constraints

To limit the scope of this project, only a single fluid phase will be considered. This may not seem like a severe restriction for a gaseous equation of state, but solid products like soot are common in the combustion of hydrocarbon molecules. Such products require their own equations of state, a far from trivial task and also a potential source of error. Therefore, the evaluation of the equation of state cannot include very oxygen-lean, carbon-containing systems.

The equation of state will also be limited to supercritical temperatures only. This guarantees that no condensation into liquid occurs, regardless of pressure. The gas-liquid coexistence region is also more difficult to handle computationally; a more complex Monte Carlo scheme is required.

Chapter 2.

Theory

2.1. The exponential-6 potential

The interactions between atoms and molecules in a fluid are determined by their intermolecular forces. This is commonly defined by an intermolecular potential, a function which describes the potential energy of two particles as function of their relative positions. One such model is the exponential-6 potential (equation 2.1). Although it strictly describes a fluid of identical, spherically symmetric particles like argon, it has been widely used to model systems of nonspherical molecules as well as mixtures of different species [19]. The exponential-6 expression of intermolecular potential energy u in a pair of particles is

$$\begin{aligned} u(r) &= \frac{\varepsilon}{\alpha - 6}\left(6\, e^{\alpha(1-r/r_m)} - \alpha\left(\frac{r_m}{r}\right)^6\right),\ r \geq r_c \\ u(r) &= \infty,\ r < r_c\ . \end{aligned} \tag{2.1}$$

where r is the distance between the particles. Every chemical species is described by a unique set of three parameters: ε is the depth of the attractive well and has units of energy, r_m is the distance where this minimum is located and α is a dimensionless parameter controlling the stiffness of repulsion at short ranges. The adjustable repulsive stiffness gives it an advantage over the commonly used Lennard-Jones potential [13], since it is an important property in very high density systems [18].

The shape of the potential is shown in figure 2.1 (a). Since the repulsive (exponential) part of the expression has a constant value at $r = 0$ but the attractive part diverges to $-\infty$, the potential has an unphysical well at very short distances. This is solved by adding a hard core with infinite potential at distances shorter than r_c, the highest point of the potential, as shown in figure 2.1 (b).

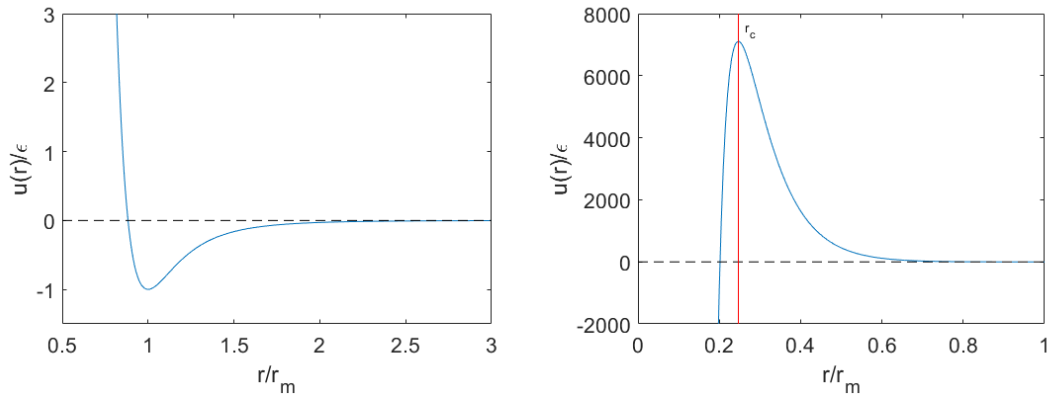

(a) Attractive region. **(b)** Repulsive region.

Figure 2.1. Graphs of the exp-6 potential in units of ε and r_m. The stiffness $\alpha = 13$. The potential energy is set to infinity for distances below r_c. Note the different scales in the subfigures.

2.1.1. Dipole approximation

Water is a particularly difficult molecule to model and the exp-6 potential is not well suited at ambient temperatures. The problem is twofold: its strongly polar nature is not captured by a spherically symmetric potential, and multi-body interactions have a significant contribution to its properties [25]. At higher temperatures, faster rotation of the molecules disrupts the hydrogen bonding and complexes. It was also shown that high pressure leads to a behaviour more similar to spherically symmetric molecules.

Based on these observations, Ree averaged the quantum mechanical pair potential of two water molecules over all rotational configurations to produce a temperature-dependent, spherically symmetric potential. This approximation successfully reproduced the measured properties of shock-compressed water [25]. In a later work, he adapted the temperature-dependent behaviour to the much simpler exp-6 potential in the form of a correction for the well depth ε [16].

$$\varepsilon = \varepsilon^0 \left(1 + \frac{\lambda}{T}\right) \tag{2.2}$$

Here, ε^0 is the potential well depth at infinite temperature, and λ controls how much the well depth increases at low temperatures.

2.2. Mixing rules

Since the interaction of many different chemical species is very complex, the mixture is treated as an effective simple fluid using the van der Waals one-fluid (vdW1f) mixing rules. An improved set of rules for the exp-6 potential was proposed by Ree [17] and is a weighted average of all the interacting species' parameters:

$$\begin{aligned} r_m^3 &= \frac{1}{n_{tot}^2} \sum_{i,j} n_i n_j r_{m,ij}^3 \\ \varepsilon &= \frac{1}{r_m^3} \frac{1}{n_{tot}^2} \sum_{i,j} n_i n_j \varepsilon_{ij} r_{m,ij}^3 \\ \alpha &= \frac{1}{r_m^3 \, \varepsilon} \frac{1}{n_{tot}^2} \sum_{i,j} n_i n_j \varepsilon_{ij} r_{m,ij}^3 \alpha_{ij} \, . \end{aligned} \tag{2.3}$$

n_i is the number of moles of the i:th species, and n_{tot} is the total number of moles of gas in the system. The parameters for two unlike species i and j are given by the extended Lorentz-Berthelot combination rule [26]:

$$\begin{aligned} r_{m,ij} &= k_{ij} \frac{r_{m,i} + r_{m,j}}{2} \\ \varepsilon_{ij} &= \sqrt{\varepsilon_i \varepsilon_j} \\ \alpha_{ij} &= \sqrt{\alpha_i \alpha_j} \, . \end{aligned} \tag{2.4}$$

Here, k_{ij} is a correction factor that enables finer tuning of gas mixtures if they are not sufficiently well represented by this mixing rule. It is equal to 1 for nearly all pairs of gases i and j. α_i, ε_i and $r_{m,i}$ are the parameters for the i:th species.

ε_i is given by the dipole approximation:

$$\varepsilon_i = \varepsilon_i^0 \left(1 + \frac{\lambda_i}{T} \right) \, , \tag{2.5}$$

where λ_i is zero for all nonpolar molecules.

2.3. Helmholtz free energy expression

The equation of state is based on an analytical expression for the excess Helmholtz free energy of the gas mixture. "Excess" here means that it is the non-ideal component of the free energy, $A^{ex} = A - A^{ideal}$. Using the mixing rules and reduced properties, the free energy can be reduced from a very complex expression to a three variable function $F(\alpha, T^*, \rho^*)$. F is scaled by the number of particles N, Boltzmann constant k_B and temperature to make it dimensionless:

$$A^{ex}(V, T, \{n_i\}, \{r_{m,i}\}, \{\varepsilon_i\}, \{\alpha_i\}) = F(\alpha, T^*, \rho^*)\, N k_B T \ . \tag{2.6}$$

Since the one-fluid parameter α is already a dimensionless quantity, only the temperature and density need to be scaled. The average potential well depth ε is used for the reduced temperature and r_m^3 is used for the reduced density:

$$\begin{aligned} T^* &= T k_B / \varepsilon \\ \rho^* &= N r_m^3 / V \ . \end{aligned} \tag{2.7}$$

The reduced density is essentially the number of particles inside a cube with side length equal to the particle's diameter.

2.3.1. Boundaries and variable transformation

Next, α, T^* and ρ^* are transformed into three new variables α_ℓ, τ and ζ.

$$\begin{aligned} \alpha_\ell &= \ln(\alpha - 9) \\ \tau &= \ln T^* \\ \zeta &= \exp(\Theta \rho^*) \ , \end{aligned} \tag{2.8}$$

where Θ is defined by

$$\Theta = \left(\frac{\alpha - \tau}{\alpha}\right)^3 + 0.000167\ T^* + 0.074\ \frac{\alpha - 10}{\sqrt{T^*}} \ . \tag{2.9}$$

The transformation fulfils two criteria: it makes the free energy easier to accurately represent with a low-order polynomial, and turns the region of interest into a cuboid. Since the α, T^*-region is already a rectangle, α_ℓ and τ may only be functions of α and T^* respectively. Logarithms were suitable, since the most rapid free energy change is at low temperatures and low α (soft systems).

The ζ-transformation was chosen so that ζ_{max} approximately matches the freezing density of the exp-6 fluid at low to medium temperatures ($2 \leq T^* \leq 15$). This was determined by Vörtler et al. through MD simulations of 500 particles, with careful

monitoring of the fluid structure to detect if solid nuclei started to form [24]. At reduced temperatures between 20 and 160, ζ_{max} approximates $z = 1.8$ which is sufficient for all shock phenomena that Suceska et al. considered [21]. For $T^* \geq 100$, ζ_{max} is chosen to limit the pressure of nitrogen gas to 2 megabar (200 GPa) which should be sufficient for all intended applications of the EOS.

The lower and upper α-limits are 10.8 and 15.5 respectively. This range includes all values for gases in the EXP6 Library by Fried et al. [14], plus an additional margin to allow for adjustments. The lower T^*-limit is based on critical point calculations for an exp-6 fluid performed by Kataoka [27]. The dimensionless critical temperature is 2.05 for a fluid with $\alpha = 10$, 1.35 for $\alpha = 14.34$ and 0.98 for $\alpha = 30$. Extrapolating from these results, $T^* \geq 1.5$ should avoid the liquid region for most common gases and gas mixtures. This limit corresponds to about 160 K for air. The upper temperature limit $T^* = 300$ is more arbitrary since ε varies widely for different gases. $T^* = 300$ corresponds to hydrogen gas at about 10 000 K, air at 31 000 K and water at 95 000 K, which should again be sufficient for all intended applications.

The Chebyshev polynomial interpolation requires variables between -1 and 1, so α_ℓ, τ and ζ are scaled to fit the interval:

$$\begin{aligned} \tilde{\alpha} &= \left(2\alpha_\ell - \alpha_{\ell,max} - \alpha_{\ell,min}\right) / \left(\alpha_{\ell,max} - \alpha_{\ell,min}\right) \\ \tilde{\tau} &= \left(2\tau - \tau_{max} - \tau_{min}\right) / \left(\tau_{max} - \tau_{min}\right) \\ \tilde{\zeta} &= \left(2\zeta - \zeta_{max} - \zeta_{min}\right) / \left(\zeta_{max} - \zeta_{min}\right) \ . \end{aligned} \tag{2.10}$$

The minimum and maximum values are given in the table below.

Table 2.1. The α_ℓ, τ and ζ limits used to scale the variables.

	min	max
α_ℓ	0.58778	1.87181
τ	0.4055	5.7038
ζ	1	6.372

Finally, the equation of state is given by the following expression for the dimensionless excess free energy:

$$F = \Phi \rho^* \ , \tag{2.11}$$

where Φ is a Chebyshev polynomial of the three scaled variables.

$$\Phi = \sum_{i=0}^{L-1} \sum_{j=0}^{M-1} \sum_{k=0}^{N-1} T_i(\tilde{\alpha}) T_j(\tilde{\tau}) T_k(\tilde{\zeta}) C_{ijk} \tag{2.12}$$

2.3.2. Chebyshev polynomials

The trivariate polynomial Φ is based on Chebyshev polynomials, which are defined as

$$T_n(x) = \cos(n \arccos(x)) \ , \tag{2.13}$$

where n is the order of the polynomial [28]. The five lowest order polynomials are shown in figure 2.2. An alternative definition, which is the one used for all numerical calculations in this work, is

$$\begin{aligned} T_0(x) &= 1 \\ T_1(x) &= x \\ T_{n+1}(x) &= 2xT_n(x) - T_{n-1}(x) \ . \end{aligned} \tag{2.14}$$

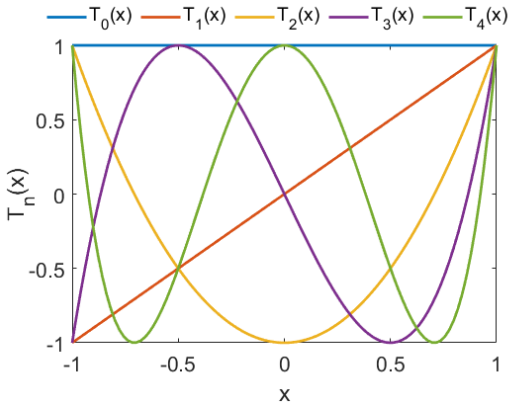

Figure 2.2. The first five Chebyshev polynomials.

Chebyshev polynomials were also used for the Monte Carlo data fitting and smoothing. Several properties make them suitable for these tasks. The polynomials are orthogonal and form a basis over the interval $[-1, 1]$. Furthermore, they are orthogonal when evaluated at the roots of a higher-order Chebyshev polynomial [28].

$$\sum_{i=1}^{N} T_m(x_i)T_n(x_i) = \begin{cases} 0 & \text{if } n \neq m \\ N & \text{if } n = m = 0 \\ N/2 & \text{if } n = m \neq 0 \end{cases} \tag{2.15}$$

Here, x_i is given by

$$x_i = \cos\left(\pi \frac{2i-1}{2N}\right) , \quad i = 1 \dots N. \tag{2.16}$$

x_i are the roots of a Chebyshev polynomial of order N, known as Chebyshev points or nodes. This set of points is particularly useful for polynomial interpolation on the

interval $[-1, 1]$, since it minimises the error. Uniformly spaced interpolation points can cause large errors close to the endpoints. The Chebyshev nodes on the other hand are distributed unevenly with more weight at the endpoints, which spreads the error uniformly over the whole interval [29].

The simplicity of data smoothing using Chebyshev smoothing is also noteworthy. Aspnes showed that even very noisy data can be used to reproduce a function correctly, by fitting an exact Chebyshev polynomial to the data points and then simply truncating the polynomial [28]. This method has been used extensively in this work to process the inherently noisy Monte Carlo data.

2.4. Derivatives

All thermodynamic properties are derived from the excess Helmholtz free energy and can be described analytically as derivatives. The derivatives are complex but straightforward; had the EOS instead been defined on the form $p(V, T)$, other properties would need to be calculated by integration which is much more difficult. This section presents the three most important properties for chemical equilibrium calculations. Once again, dimensionless quantities are used.

$$\begin{aligned} Z &= \frac{pV}{Nk_BT} \\ U^* &= \frac{U^{ex}}{Nk_BT} \\ \mu_i^* &= \frac{\mu_i^{ex}}{RT} \end{aligned} \tag{2.17}$$

Here, Z is the compressibility factor – the deviation from ideal gas behaviour, U^{ex} is the excess internal energy, and μ_i^{ex} is the excess chemical potential of the i:th species. Their relationships with the free energy are as follows:

$$Z = 1 + \rho \left(\frac{\partial F}{\partial \rho} \right)_{T,\{n_i\}} \tag{2.18}$$

$$U^* = -T \left(\frac{\partial F}{\partial T} \right)_{\rho,\{n_i\}} \tag{2.19}$$

$$\mu_i^{ex} = \left(\frac{\partial A^{ex}}{\partial n_i} \right)_{T,V,\{n_{j\neq i}\}} = \frac{\rho}{n_{tot}} \left(\frac{\partial A^{ex}}{\partial \rho} \right)_{T,\{n_i\}} + \left(\frac{\partial A^{ex}}{\partial n_i} \right)_{T,\rho,\{n_{j\neq i}\}} . \tag{2.20}$$

Adopting the compact notation for partial derivatives from [19], the derivatives of a function $f(T, \rho, \{n_i\})$ will henceforth be written as:

$$\begin{aligned} f_T &\equiv \left(\frac{\partial f}{\partial T}\right)_{\rho,\{n_i\}} \\ f_\rho &\equiv \left(\frac{\partial f}{\partial \rho}\right)_{T,\{n_i\}} \\ f_{n_i} &\equiv \left(\frac{\partial f}{\partial n_i}\right)_{T,\rho,\{n_{j\neq i}\}} . \end{aligned} \tag{2.21}$$

Since functions of transformed variables will be extensively used, the same notation is also used for derivatives of α, τ, and ζ.

$$\begin{aligned} g_\alpha &\equiv \left(\frac{\partial g}{\partial \alpha}\right)_{\tau,\zeta} \\ g_\tau &\equiv \left(\frac{\partial g}{\partial \tau}\right)_{\alpha,\zeta} \\ g_\zeta &\equiv \left(\frac{\partial g}{\partial \zeta}\right)_{\alpha,\tau} \end{aligned} \tag{2.22}$$

In this shorthand notation, the expression for the compressibility factor Z is simply:

$$\begin{aligned} Z &= 1 + \rho F_\rho \\ &= 1 + \rho \left(\Phi_\rho \rho^* + \Phi b\right) . \end{aligned} \tag{2.23}$$

b is defined in equation 2.31. The dimensionless excess internal energy is

$$\begin{aligned} U^* &= -T F_T \\ &= -\rho^* T \Phi_T , \end{aligned} \tag{2.24}$$

and the excess chemical potential is given by:

$$\mu_i^{ex} = \frac{\rho}{n_{tot}} \left(F n_{tot} RT\right)_\rho + \left(F n_{tot} RT\right)_{n_i} . \tag{2.25}$$

The chemical potential is made dimensionless by division by RT.

$$\begin{aligned} \mu_i^* &= \rho F_\rho + n_{tot} F_{n_i} + F \\ &= Z - 1 + F + n_{tot}\, \rho^* \left(\Phi_{n_i} + \Phi \frac{b_{n_i}}{b}\right) \end{aligned} \tag{2.26}$$

The three derivatives of Φ are:

$$\begin{aligned}
\Phi_T &= \Phi_{\alpha_\ell}\frac{1}{\alpha-9}\alpha_T + \Phi_\tau\tau_T + \Phi_\zeta\zeta_T \\
\Phi_\rho &= \Phi_\zeta\zeta_\rho \\
\Phi_{n_i} &= \Phi_{\alpha_\ell}\frac{1}{\alpha-9}\alpha_{n_i} + \Phi_\tau\tau_{n_i} + \Phi_\zeta\zeta_{n_i}\ .
\end{aligned} \tag{2.27}$$

Since Φ is a sum of Chebyshev polynomials of $\tilde{\alpha}$, $\tilde{\tau}$, and $\tilde{\zeta}$, the α_ℓ, τ, and ζ-derivatives are calculated simply by differentiating the appropriate polynomial in each term of the sum. Φ_ζ is shown below as example.

$$\Phi_\zeta = \frac{2}{\zeta_{max}-\zeta_{min}}\sum_{i=0}^{L-1}\sum_{j=0}^{M-1}\sum_{k=0}^{N-1}T_i(\tilde{\alpha}_n)T_j(\tilde{\tau}_n)\frac{\mathrm{d}T_k(\tilde{\zeta})}{\mathrm{d}\tilde{\zeta}}C_{ijk} \tag{2.28}$$

The derivatives of ζ are given below.

$$\begin{aligned}
\zeta_T &= \rho^*\zeta\left(\Theta_\tau\tau_T + \Theta_\alpha\alpha_T\right) \\
\zeta_\rho &= \Theta\zeta b \\
\zeta_{n_i} &= \rho^*\zeta\left(\Theta_\alpha\alpha_{n_i} + \Theta_\tau\tau_{n_i} + \Theta\frac{b_{n_i}}{b}\right)
\end{aligned} \tag{2.29}$$

Θ is a function of α and τ and its derivatives are

$$\begin{aligned}
\Theta_\tau &= -\frac{3(\alpha-\tau)^2}{\alpha^3} + 0.000167\ T^* - 0.037\ \frac{\alpha-10}{\sqrt{T^*}} \\
\Theta_\alpha &= \frac{3(\alpha-\tau)^3}{\alpha^4} + \frac{3(\alpha-\tau)^2}{\alpha^3} + \frac{0.074}{\sqrt{T^*}}\ ,
\end{aligned} \tag{2.30}$$

which are expressed using a combination of τ and T^* for numerical efficiency. Next, a, b and c are defined based on the mixing rules:

$$\begin{aligned}
a = \varepsilon r_m^3 &= \frac{1}{n_{tot}^2}\sum_{i,j} n_i n_j \varepsilon_{ij} r_{m,ij}^3 \\
b = r_m^3 &= \frac{1}{n_{tot}^2}\sum_{i,j} n_i n_j r_{m,ij}^3 \\
c = \alpha\varepsilon r_m^3 &= \frac{1}{n_{tot}^2}\sum_{i,j} n_i n_j \varepsilon_{ij} r_{m,ij}^3 \alpha_{ij}\ .
\end{aligned} \tag{2.31}$$

Those are used to simplify the derivatives of α and τ:

$$\begin{aligned} \alpha_T &= \frac{c_T}{a} - \frac{c a_T}{a^2} \\ \alpha_{n_i} &= \frac{c_{n_i}}{a} - \frac{c a_{n_i}}{a^2} \end{aligned} \tag{2.32}$$

$$\begin{aligned} \tau_T &= \frac{1}{T} - \frac{a_T}{a} \\ \tau_{n_i} &= \frac{b_{n_i}}{b} - \frac{a_{n_i}}{a} \ . \end{aligned} \tag{2.33}$$

Finally, the derivatives of a, b and c are

$$\begin{aligned} a_T &= \frac{1}{n_{tot}^2} \sum_{i,j} n_i n_j r_{m,ij}^3 \frac{\mathrm{d}\varepsilon_{ij}}{\mathrm{d}T} \\ c_T &= \frac{1}{n_{tot}^2} \sum_{i,j} n_i n_j r_{m,ij}^3 \alpha_{ij} \frac{\mathrm{d}\varepsilon_{ij}}{\mathrm{d}T} \ , \end{aligned} \tag{2.34}$$

where

$$\frac{\mathrm{d}\varepsilon_{ij}}{\mathrm{d}T} = -\frac{\varepsilon_i^0 \varepsilon_j^0 \left(T(\lambda_i + \lambda_j) + 2\lambda_i \lambda_j\right)}{2T^2 \sqrt{\varepsilon_i^0 \varepsilon_j^0 (T + \lambda_i)(T + \lambda_j)}} \tag{2.35}$$

and $b_T = 0$. The n_i-derivatives are:

$$\begin{aligned} a_{n_i} &= \frac{2}{n_{tot}^2} \sum_j n_j \varepsilon_{ij} r_{m,ij}^3 - \frac{2a}{n_{tot}} \\ b_{n_i} &= \frac{2}{n_{tot}^2} \sum_j n_j r_{m,ij}^3 - \frac{2b}{n_{tot}} \\ c_{n_i} &= \frac{2}{n_{tot}^2} \sum_j n_j \varepsilon_{ij} r_{m,ij}^3 \alpha_{ij} - \frac{2c}{n_{tot}} \ . \end{aligned} \tag{2.36}$$

2.5. Shock theory and the detonation wave

Data from shock compression experiments and detonation measurements have been used extensively throughout this project. This section gives a brief introduction to the theory behind the reactive and unreactive one-dimensional shock wave.

A plane shock wave can be described by the Rankine–Hugoniot relations, which relate the conditions before and after the shock wave. For initially stationary media, the following three equations describe the conservation of mass, momentum and energy respectively [30]:

$$V_1/V_0 = \frac{u_s - u_p}{u_s} \tag{2.37}$$

$$p_1 - p_0 = \frac{u_s\, u_p}{V_0} \tag{2.38}$$

$$U_1 - U_0 = \frac{1}{2}\ (p_1 + p_0)\,(V_0 - V_1)\ , \tag{2.39}$$

where V is the specific volume $(1/\rho)$, the subscripts 0 and 1 indicate conditions in the unshocked respectively shocked material, u_s is the shock velocity and u_p is the particle or mass velocity.

From an experimental point of view, this means that the properties of the shocked media can be determined by measuring u_s and u_p only [30]. Typically, the shock wave is produced by hitting the sample with a high velocity projectile from a light gas gun [31], a high intensity laser pulse [32] or the shock wave from a high explosive [30]. The shock velocity is measured directly and the mass velocity is given by impedance matching [31]. V_0 and p_0 are known from the density of the sample and the ambient pressure, so the shock pressure and compressed specific volume are given by equations 2.37 and 2.38.

From a computational viewpoint, it is easier to express u_s and u_p as functions of p and V:

$$u_s = V_0\sqrt{\frac{p_1 - p_0}{V_0 - V_1}} \tag{2.40}$$

$$u_p = V_0\frac{p_1 - p_0}{u_s}\ . \tag{2.41}$$

Given a volume V_1, the shock pressure can be calculated iteratively by guessing a pressure p_1 and then:

- Calculate U_1 using equation 2.39.
- Calculate a temperature T_1 which matches the internal energy.
- Calculate a new pressure at V_1 and T_1 using an equation of state.

The system rapidly converges at the correct p_1. If the temperature and pressure are high enough to dissociate the media, chemical equilibrium must be calculated in the loop as well. The function $p_1(V_1)$ is known as the shock Hugoniot.

The key difference between a general shock wave and a detonation wave is that the detonation wave is self sustaining, due to the release of chemical energy behind the shock front. Each explosive or reactive gas mixture has its own unique detonation properties; shock velocity, pressure, temperature; that are related to its density, composition and energy content. The simplest model is the Chapman–Jouguet detonation wave which is outlined below.

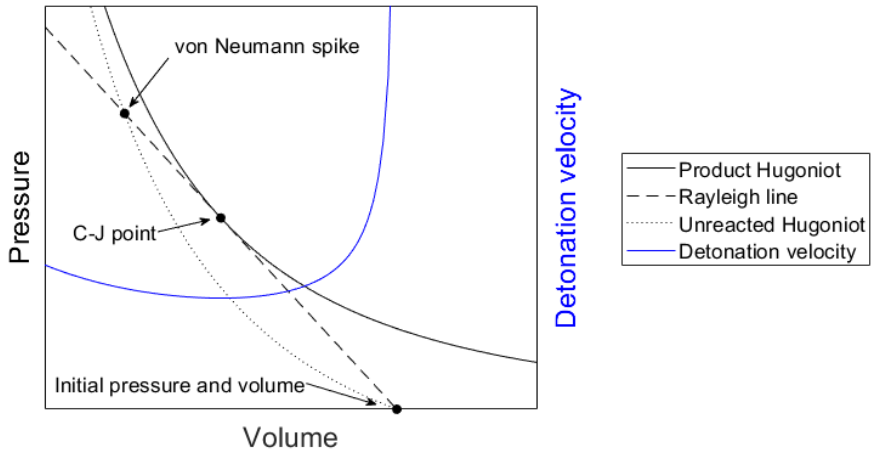

Figure 2.3. Typical shock Hugoniots for explosives and detonation products. The Rayleigh line connects the initial state with the states in the von Neumann spike and C-J point. The detonation velocity as function of the volume V_1 is also shown in blue.

The combustible gas mixture or high explosive is initially at rest when the shock wave arrives. The shock wave compresses the material along the unreacted Hugoniot to a high-pressure state called the von Neumann spike [33], shown in figure 2.3. This marks the beginning of the exothermic reaction zone and the reaction progresses as the gases expand along the Rayleigh line. The line is tangent to the reaction product Hugoniot at the C-J point — this is the point where the reactions are completed and chemical equilibrium is achieved [33]. The shock velocity calculated with the pressure and volume at the C-J point is the steady-state detonation velocity D_{CJ}.

For modelling purposes, another property of the C-J point can be utilised: the detonation velocity can never be lower than D_{CJ} [33]. Therefore, it is sufficient to calculate the shock Hugoniot for the reaction products, which can be done with the same iterative method as the shock waves above. Then, the point along the Hugoniot that gives the lowest detonation velocity according to equation 2.40 is the C-J point.

2.6. Monte Carlo

Monte Carlo methods are a class of computational methods that are based on random sampling. They are well suited to perform numerical integration in high-dimensional spaces where uniform grids fail. Integrating some function using 100 evaluation points per dimension is quite feasible in one, two or three dimensions — requiring 10^2, 10^4 and 10^6 evaluations of the integrand respectively. However, this strategy is impossible in 100-dimensional space since it would require 10^{200} calculations.

The high-dimensional integrals have a direct connection to fluid simulations [3]. For N particles in the canonical ensemble (constant number of particles, constant temperature and constant volume), the equilibrium value of a quantity A is

$$\langle A \rangle = \frac{\int A \, e^{-\beta E} \mathrm{d}^{3N} p \, \mathrm{d}^{3N} r}{\int e^{-\beta E} \mathrm{d}^{3N} p \, \mathrm{d}^{3N} r} \, . \tag{2.42}$$

The integrals are taken over every possible configuration r and every possible momentum p. The weight of each state is given by the Boltzmann factor $e^{-\beta E}$, where E is the total energy of the system and $\beta = \frac{1}{k_B T}$. However, since the forces between particles only depend on their configuration, the internal energy and pressure in the system can be determined without integration over momentum-space. Still, even with as little as 100 particles, a 300-dimensional integral is far beyond what can be solved with conventional numerical integration.

The most basic Monte Carlo approach would be to randomly select a configuration, calculate the energy and weight that integration point with the Boltzmann factor [3]. This method would fail too however, due to the fact that the vast majority of configurations in a high density fluid are extremely unlikely. In fact, the probability to randomly pick a configuration with nonzero Boltzmann factor for 100 hard-sphere particles at their freezing point is 10^{-260} [4].

Metropolis et al. [3] therefore proposed a different scheme with one critical difference:

"instead of choosing configurations randomly, then weighting them with $\exp(-E/kT)$, we choose configurations with a probability $\exp(-E/kT)$ and weight them evenly."

An analogy to highlight the difference between the basic scheme and the Metropolis scheme could be to measure the average depth of the river Nile, without knowing exactly where the Nile is. The naive method is to choose random sampling points over the whole African continent, measure the depth, and give the measurement a weight 1 if it was taken in the Nile and 0 otherwise. The Metropolis scheme instead constructs a random walk through the river. With a starting point somewhere close to the Nile, each step consists of a short random trial move which is accepted if it lands in the river and rejected otherwise. When the river has been reached, each trial move is followed by a depth measurement, either at the newly accepted position or once more at the old position if a

move was rejected. Every measurement is weighted equally [4].

The same principle is applied to particles in a box in order to compute the equilibrium properties of a fluid. The particles are initially placed in some allowed configuration, i.e. with no overlapping hard cores [4]. This could for example be a cubic lattice. Then, a particle is selected and given a random displacement. If the total energy of the system decreased due to the trial move, the move is accepted. If the energy increased, the move is accepted with probability $\exp(-\beta\Delta E)$ where ΔE is the energy change. The particle is moved back to its previous position if the move is rejected [3]. Finally, the desired properties of the system are sampled and the procedure can be repeated with new particles, until enough samples have been collected to produce an accurate average.

There is an obvious size difference between a box containing a few hundred particles and a real fluid system, for example a drop of water consisting of 10^{21} molecules. In order to avoid surface effects from the tiny box, the walls are periodic boundaries [3] as shown in figure 2.4. The simulation box is essentially surrounded by copies of itself, and real particles in the box can interact with images of other particles. The distance from one particle to another is defined as the distance to the closest copy of the other particle [3]. Each particle only interacts once with every unique particle and interactions with copies further away are ignored, a sufficient approximation for intermolecular potentials without long range components [3]. The distance at which interactions are no longer considered is called the cutoff distance, denoted r_{cut}. This is usually half the box side length or shorter in the case of a low-density fluid.

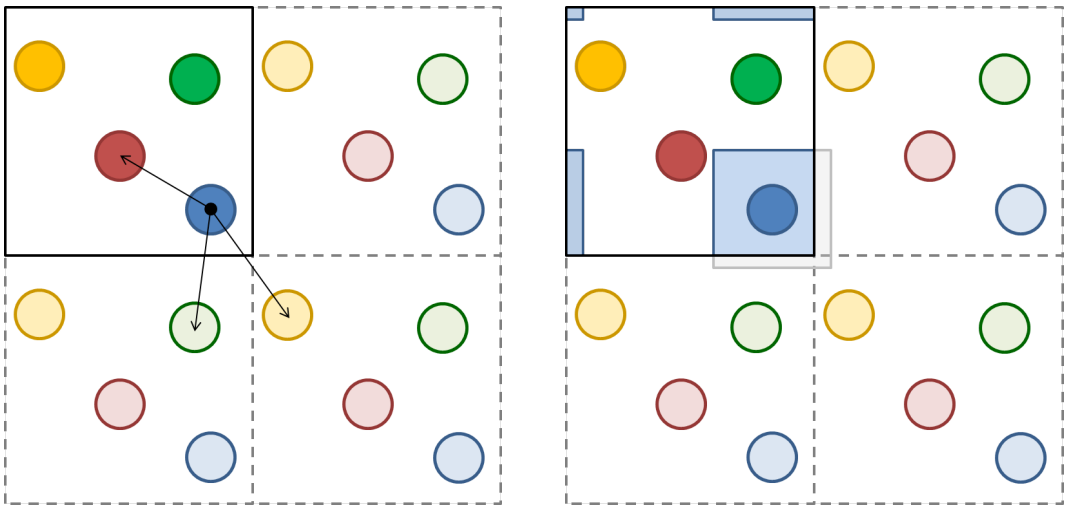

(a) The distance between any two particles A and B is always the shortest distance between A and any image of B.

(b) A particle will always stay within the "real" box during a trial move; the blue (split) square is valid destinations.

Figure 2.4. The periodic nature of the simulation is shown for the 2-dimensional case. The solid box is the "real" box and the dashed boxes are the periodic images.

The two desired thermodynamic properties in this work are the internal energy of the system and the compressibility factor, which is calculated from the pressure. The internal energy U per particle is simply the average energy of each configuration divided by the number of particles,

$$U = \frac{1}{N}\overline{E} \ . \tag{2.43}$$

The pressure of the system is given by:

$$p = \frac{Nk_BT}{V} + \frac{1}{3V}\overline{\sum_{i<j} \mathbf{f}_{ij}\mathbf{r}_{ij}} \tag{2.44}$$

where the first term is the ideal gas contribution and the second term is the virial [34]. $\mathbf{f}_{ij}$ is the intermolecular force that particle j applies to particle i, and $\mathbf{r}_{ij}$ is the vector from i to j. For the spherically symmetric exp-6 potential, $\mathbf{f}_{ij}\mathbf{r}_{ij}$ simplifies to

$$\mathbf{f}_{ij}\mathbf{r}_{ij} = \frac{6\alpha\varepsilon}{\alpha - 6}\left(\frac{r_{ij}}{r_m}e^{\alpha(1-r_{ij}/r_m)} - \left(\frac{r_m}{r_{ij}}\right)^6\right) \ , \tag{2.45}$$

which can be calculated and summed at the same time as the energy above.

The contribution from particles further away than half the box is small, but not negligible. Therefore, long-range corrections based on the radial distribution function $g(r)$ are usually added to the desired properties [19]. The radial distribution function is closely tied to the structure of the fluid and describes the average density at distance r from a particle, normalised by the density of an ideal gas. Its typical shape for a high-density fluid is shown in figure 2.5 below.

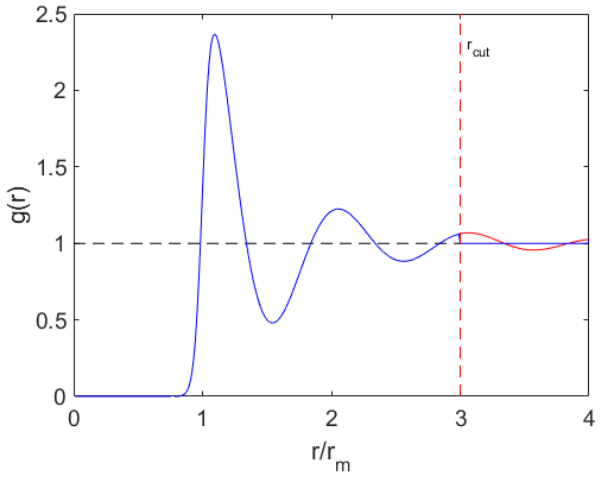

Figure 2.5. Typical radial distribution function. Long-range corrections can be calculated by setting $g(r) = 1$ outside the cutoff radius, i.e. assuming randomly distributed particles.

The internal energy and compressibility factor are completely determined by the radial distribution function in combination with the intermolecular potential $u(r)$ [19]. The following expressions apply to spherically symmetric potentials:

$$U^* = \frac{2\pi\rho}{k_B T} \int_0^\infty u(r) g(r) r^2 \mathrm{d}r \ . \tag{2.46}$$

$$Z = 1 - \frac{2\pi\rho}{3k_B T} \int_0^\infty r \frac{\mathrm{d}u(r)}{\mathrm{d}r} g(r) r^2 \mathrm{d}r \ , \tag{2.47}$$

By approximating $g(r) = 1$ for $r > r_{cut}$, as shown in figure 2.5, these expressions can be used to generate the long-range correction terms U_{tail} and Z_{tail}:

$$\begin{aligned} U_{tail} &= -\frac{2\pi\rho^*}{T^*} \int_{r_{cut}}^\infty \frac{1}{\alpha - 6} \left(6e^{\alpha(1-r^*)} - \alpha r^{*-6} \right) r^{*2} \mathrm{d}r^* \\ &\approx -\frac{2\alpha\pi\rho^*}{3(\alpha - 6) T^* r_{cut}^3} \end{aligned} \tag{2.48}$$

$$\begin{aligned} Z_{tail} &= -\frac{2\pi\rho^*}{3T^*} \int_{r_{cut}}^\infty \frac{6\alpha}{\alpha - 6} \left(-r^* e^{\alpha(1-r^*)} + r^{*-6} \right) r^{*2} \mathrm{d}r^* \\ &\approx -\frac{4\alpha\pi\rho^*}{3(\alpha - 6) T^* r_{cut}^3} \ , \end{aligned} \tag{2.49}$$

where $r^* = r/r_m$. The analytical expressions are achieved by ignoring the exponential term in the integrals, a fair approximation since it contributes with less than 0.0001% of the total integral.

Chapter 3.

Method

3.1. Monte Carlo implementation

A basic Monte Carlo program was written in C to simulate an exp-6 fluid in the canonical ensemble. The program calculates the excess internal energy and the compressibility factor of the fluid given a reduced temperature, reduced density and stiffness coefficient. It was implemented in less than 250 lines of code, following the basic algorithm presented in section 2.6.

An important problem caused by the choice of language lies in the generation of pseudorandom floating-point numbers. The built-in rand function in C generates integers, varies with implementation and is of questionable quality (rand_max is specified to be as small as 32767)[35]. The Mersenne Twister was chosen instead. It is the standard PRNG in many other common programming languages [36] and should be sufficient for this task. In particular, a C implementation of the Mersenne Twister by Evan Sultanik [37] was used. Each run started by seeding the PRNG with the current time, followed by 100000 iterations to improve the random quality.

Initialisation is done by placing N particles (usually 512, always a cube number) in a box with side length $L = \sqrt[3]{N/\rho^*}$. The particles are defined by a 2D array of coordinates and spaced evenly in a cubic lattice. The cutoff distance r_{cut} is set to $\min(3, L/2)$ and the hard sphere-distance (which only depends on α) is solved iteratively.

The periodic boundaries are enforced by two different functions: one for particle positions, and one for distances between particles. If a trial move would take a particle outside the allowed $[0, L)$ interval in any direction, L is added or subtracted to let the particle reappear on the opposite side of the box. A single addition or subtraction is guaranteed to bring it back into the box since the maximum displacement in a move is always smaller than L. The other function is applied during every particle interaction. A particle will always only interact with the closest version of another particle, either the "real" particle or one of its periodic images outside the box. Thus, the components of the vector between them must fall within the interval $[-L/2, L/2)$. This is solved by adding or subtracting L if needed.

Before the main loop, the total energy and virial of the system are calculated by the energy function. The function starts by setting the energy and virial to zero. It then loops over each unique pair of particles and calculates the square of the distance between them as $d^2 = \Delta x^2 + \Delta y^2 + \Delta z^2$. If d^2 is smaller than r_{cut}^2, their potential energy and virial contribution are calculated and added. The particles are guaranteed to never be within the hard-sphere distance from each other when the energy function is called so it does not have to check for that case.

The main loop runs for a set number of cycles, each one consisting of N trial moves. A trial move starts by picking a particle i at random. Next, an array with the new trial coordinates is created by taking the old coordinates and adding a random displacement $\delta r(\xi_1, \xi_2, \xi_3)$ where ξ_n are independent uniformly distributed random numbers in the $[-1, 1]$ interval and δr is the maximum displacement. After correction for periodic boundaries, the energy change resulting from the move is calculated using the deltaEnergy function. This step is by far the most computationally intensive and required the most thorough optimisation.

The deltaEnergy function starts by setting the energy change dU and virial change $dVir$ to zero. It then loops over every particle $j \neq i$. For each particle, the vector between i and j is calculated for both i's old and trial coordinates and the six values are stored in a single array. The periodic boundaries are applied to the vector, this time inlined to avoid function overhead. Next, the trial move distance squared and the old distance squared are calculated and stored at positions 0 and 1 in an array r. If the trial position is outside the hard-sphere distance and within the cutoff distance, its contribution to dU and $dVir$ is calculated by the following code:

```
r[2] = sqrt(r[0]); //trial distance
r[3] = sqrt(r[1]); //old distance
r[4] = exp(alpha-alpha*r[2]); //repulsive part
r[5] = exp(alpha-alpha*r[3]);
r[6] = 1/(r[0]*r[0]*r[0]); //attractive part
r[7] = 1/(r[1]*r[1]*r[1]);

dU += 6/alpha*(r[4]-r[5]) - r[6] + r[7]; //energy
dVir += r[2]*r[4] - r[6] - r[3]*r[5] + r[7]; //virial
```

Although almost unreadable, it is extremely fast. The array guarantees that all values are stored on adjacent memory cells. The expensive pow() is avoided and exp(), which uses the majority of the time in the program, is only performed once per interaction instead of twice like in the energy function. If the trial distance is shorter than the hard-sphere distance, the function is immediately terminated and the trial move is rejected. After the loop, dU and $dVir$ are multiplied by $\alpha/(\alpha - 6)$ and $6\alpha/(\alpha - 6)$ before returning the results.

Back to the main loop, the trial move is accepted if $\exp(-dU/T^*) > \xi$, where ξ is a random number in the $[0, 1]$ range. If accepted, the old coordinates in the coordinate array are replaced by the trial coordinates. The energy and virial of the system are

updated by adding dU and $dVir$. The data collection starts after a predetermined number of equilibrium cycles (usually 5000) has passed. The energy and virial are sampled after each trial move, regardless of whether it was accepted or not, in order to calculate averages at the end of the simulation.

The maximum step size δr is adjusted during the first 50 cycles of the simulation. A larger step size leads to fewer accepted trial moves and the goal is a 50% acceptance rate. The following proportional controller is used:

$$\delta r_{n+1} = \delta r_n \left(0.8 + 0.4\frac{A}{N}\right) , \tag{3.1}$$

where A is the number of accepted moves during the last cycle of N attempted moves. The maximum allowed step size is $\alpha/120$ if $\rho^* < 2$ and 0.4 for higher densities. These settings gave good convergence rate and accuracy.

After the program has run the desired number of data collection cycles, the internal energy and virial averages are calculated. The final internal energy and compressibility factor are printed after U_{tail} and Z_{tail} have been added.

3.2. Monte Carlo simulations

The simulations were performed on NSC's cluster Tetralith, part of the Swedish National Infrastructure for Computing (SNIC). Thanks to the cubic domain of interest and the predefined Chebyshev nodes, the question was not where in $\alpha\rho^*T^*$-space to perform Monte Carlo simulations, but simply how many and whether splitting the domain would be necessary. Initial testing with 1000 points in a single domain showed that the behaviour in τ-direction was too complex to allow for efficient smoothing, so the region of interest was split into 16 equally sized domains — eight in the τ-direction and two in the α_ℓ-direction. Keeping the domains continuous in the ζ-direction was necessary to simplify the integration during post-processing.

The uncertainty in a MC simulation decreases with the square of the number of cycles, i.e. doubling the accuracy requires four times more computational power. The same computing time could be used to run four MC simulations instead. The problem is illustrated in figure 3.1. The left graph shows a reference function $y = x^2$ and three points with an added random normally distributed error ($\sigma = 0.1$). The green curve shows the exact second order fit to those points. In the right graph, the nine points were given $\sqrt{3}$ times larger error. The exact fit is quite far from $y = x^2$, but the red curve which is smoothed by truncation to second order is similar to the green curve.

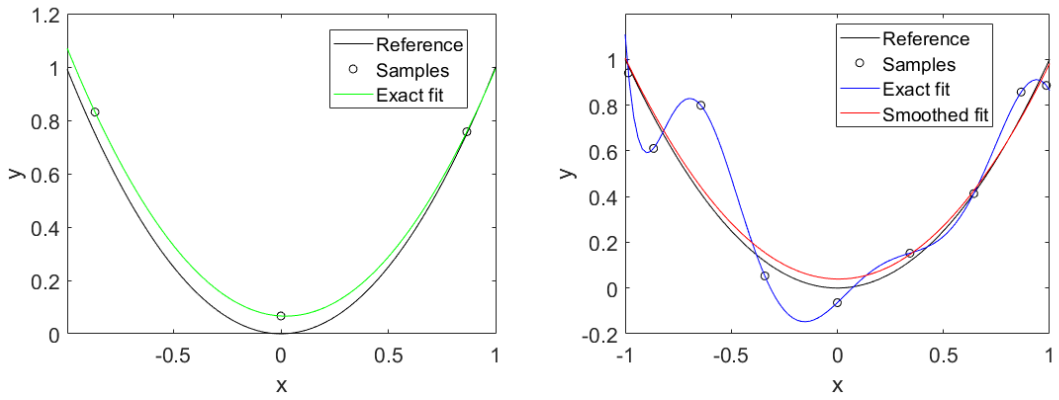

(a) Few, more accurate samples.

(b) Many, less accurate samples.

Figure 3.1. Illustration of two ways to recreate the reference function $y = x^2$ using noisy data. The total computation time would be the same in both examples if the points were MC simulations. The final polynomial fits have identical absolute errors on average.

On average, the absolute error is exactly the same for both methods, and only affected by the total computation time. Too many short simulations are counterproductive however, since each simulation starts with 5000 equilibrium cycles before the data collection phase. Too short simulations will therefore waste most of the computation time without contributing to the result. Too few long simulations on the other hand makes the smoothing process more difficult, and outliers are harder to identify.

For the full scale simulation, ten points in each direction was chosen as a compromise. In total, 16 000 MC simulations were performed with 15 000 cycles each, in roughly 1000 core-hours. About 20 outliers were identified and re-simulated with 30 000 cycles each.

3.3. Polynomial fit to Monte Carlo data

The data processing was performed in Matlab. The process can be divided into three main parts which are described in the following sections:

- Smoothing of raw Monte Carlo data,
- Integration to find Φ in each domain,
- Combination of all domains into the final equation of state.

3.3.1. Data fitting and smoothing

The raw Z and U^* data could not be used to calculate F and Φ directly due to the random noise from the inherently stochastic simulations. The noise was reduced by fitting an exact Chebyshev polynomial to the data, e.g. ninth order polynomial to ten data points, and then truncating to a lower order polynomial. To ensure that $U^* \to 0$ and $Z \to 1$ when $\rho \to 0$ (the ideal gas case), $(Z-1)/\rho^*$ and U^*/ρ^* were fitted instead of Z and U^*.

The standard matrix polynomial regression method was adapted to a three-dimensional Chebyshev polynomial. A continuous function y can be represented in the following way:

$$y(\tilde{\alpha}, \tilde{\tau}, \tilde{\zeta}) = \sum_{i=0}^{M-1} \sum_{j=0}^{M-1} \sum_{k=0}^{M-1} T_i(\tilde{\alpha}) T_j(\tilde{\tau}) T_k(\tilde{\zeta}) C_{ijk} \ . \tag{3.2}$$

With $m = M^3 = 1000$ data points y_n evaluated at unique sets of inputs $(\tilde{\alpha}, \tilde{\tau}, \tilde{\zeta})_n$, the following system of linear equations is formed:

$$\begin{bmatrix} y_1 \\ y_2 \\ \vdots \\ y_m \end{bmatrix} = \begin{bmatrix} T_0(\tilde{\alpha}_1)T_0(\tilde{\tau}_1)T_0(\tilde{\zeta}_1) & T_0(\tilde{\alpha}_1)T_0(\tilde{\tau}_1)T_1(\tilde{\zeta}_1) & \cdots & T_{M-1}(\tilde{\alpha}_1)T_{M-1}(\tilde{\tau}_1)T_{M-1}(\tilde{\zeta}_1) \\ T_0(\tilde{\alpha}_2)T_0(\tilde{\tau}_2)T_0(\tilde{\zeta}_2) & T_0(\tilde{\alpha}_2)T_0(\tilde{\tau}_2)T_1(\tilde{\zeta}_2) & \cdots & T_{M-1}(\tilde{\alpha}_2)T_{M-1}(\tilde{\tau}_2)T_{M-1}(\tilde{\zeta}_2) \\ \vdots & \vdots & \ddots & \vdots \\ T_0(\tilde{\alpha}_m)T_0(\tilde{\tau}_m)T_0(\tilde{\zeta}_m) & T_0(\tilde{\alpha}_m)T_0(\tilde{\tau}_m)T_1(\tilde{\zeta}_m) & \cdots & T_{M-1}(\tilde{\alpha}_m)T_{M-1}(\tilde{\tau}_m)T_{M-1}(\tilde{\zeta}_m) \end{bmatrix} \begin{bmatrix} c_1 \\ c_2 \\ \vdots \\ c_m \end{bmatrix} \tag{3.3}$$

or in short form,

$$\boldsymbol{y} = \mathbf{A}\boldsymbol{c} \ . \tag{3.4}$$

The coefficient vector $\boldsymbol{c}$ is found by matrix inversion,

$$\boldsymbol{c} = \mathbf{A}^{-1}\boldsymbol{y} \ . \tag{3.5}$$

Which is finally truncated to order U, V, W by setting all coefficients $C_{ijk} = 0$ if $i \geq U$ or $j \geq V$ or $k \geq W$. U and V were usually set to between 5 and 7, and W between 6 and 8. The smoothing was optimised by hand for each domain.

3.3.2. Integration

With the goal of achieving a Chebyshev representation of Φ in mind, the two relevant thermodynamic derivatives are:

$$\begin{aligned} Z &= 1 + \rho \left(\frac{\partial F}{\partial \rho} \right)_{T,\{n_i\}} \\ U^* &= -T \left(\frac{\partial F}{\partial T} \right)_{\rho,\{n_i\}} . \end{aligned} \tag{3.6}$$

The compressibility factor was used first and integrated to yield the excess free energy.

$$\begin{aligned} F &= \int_0^{\rho^*} \frac{Z(\rho^{*\prime}) - 1}{\rho^{*\prime}} \mathrm{d}\rho^{*\prime} \\ &= \int_1^{\zeta} \frac{Z(\zeta') - 1}{\zeta' \log \zeta'} \mathrm{d}\zeta' \\ &= \frac{\zeta_{max} - \zeta_{min}}{2} \int_{-1}^{\tilde{\zeta}} \frac{Z(\tilde{\zeta}')}{\zeta'(\tilde{\zeta}') \log\left(\zeta'(\tilde{\zeta}')\right)} \mathrm{d}\tilde{\zeta}' \end{aligned} \tag{3.7}$$

This expression requires a continuous integrand, so the smoothed representation of $(\boldsymbol{Z} - 1) \oslash \boldsymbol{\rho^*} = \mathbf{A}\boldsymbol{c}_z$ was used. Bold letters denote column vectors (except for $\mathbf{A}$ which is a matrix) and $\oslash$ denotes element-wise division. The integrand in the equation above was then represented by another Chebyshev polynomial using the smoothed compressibility factor $\mathbf{A}\boldsymbol{c}_z$:

$$\mathbf{A}\boldsymbol{c}_\zeta = (\mathbf{A}\boldsymbol{c}_z \circ \boldsymbol{\rho^*}) \oslash (\boldsymbol{\zeta} \circ \log \boldsymbol{\zeta}) , \tag{3.8}$$

where $\boldsymbol{\zeta}$ and $\boldsymbol{\rho^*}$ are transformed vectors corresponding to the vectors $\tilde{\boldsymbol{\alpha}}, \tilde{\boldsymbol{\tau}}$ and $\tilde{\boldsymbol{\zeta}}$. $\circ$ denotes element-wise multiplication. With the integrand as a polynomial, the analytical integral was then calculated at each of the 1000 Chebyshev nodes n to give $\boldsymbol{F}$.

$$F_n = \frac{\zeta_{max} - \zeta_{min}}{2} \sum_{i=0}^{M-1} \sum_{j=0}^{M-1} \sum_{k=0}^{M-1} T_i(\tilde{\alpha}_n) T_j(\tilde{\tau}_n) C_{\zeta,ijk} \int_{-1}^{\tilde{\zeta}_n} T_k(\tilde{\zeta}') \mathrm{d}\tilde{\zeta}' \tag{3.9}$$

Finally, a Chebyshev polynomial representation of Φ was fitted:

$$\boldsymbol{\Phi} = \mathbf{A}\boldsymbol{c}_\phi = \boldsymbol{F} \oslash \boldsymbol{\rho^*} . \tag{3.10}$$

This representation's ζ-derivative had excellent accuracy, however, small deviations in the τ-direction caused large errors in the τ-derivative. The Monte Carlo generated internal energy data was used to improve the fit.

Using the excess internal energy was not as straightforward as the compressibility factor since the relation is a partial differential equation. The temperature-derivative in equation 3.6, transformed to $\alpha\tau\zeta$-space, is given in the equation below. The shorthand notation

for partial derivatives is used again for simplicity.

$$U^* = -\Phi_\tau \rho^* - \Phi_\zeta \rho^{*2} \zeta \Theta_\tau \tag{3.11}$$

Solving for the τ-derivative of Φ:

$$\Phi_\tau = -\frac{U^*}{\rho^*} - \Phi_\zeta \rho^* \zeta \Theta_\tau \ . \tag{3.12}$$

Integration yields an expression for Φ,

$$\Phi = -\int_{\tau_{min}}^{\tau} \frac{U^*}{\rho^*} + \Phi_\zeta \rho^* \zeta \Theta_\tau \, \mathrm{d}\tau + f(\tilde{\alpha}, \tilde{\zeta}) \ , \tag{3.13}$$

where $f(\tilde{\alpha}, \tilde{\zeta})$ is an arbitrary function independent of τ. This is not an explicit expression, so the previously generated representation of Φ was used to calculate the ζ-derivative of Φ in the integral above.

$$\Phi_\zeta = \frac{2}{\zeta_{max} - \zeta_{min}} \sum_{i=0}^{M-1} \sum_{j=0}^{M-1} \sum_{k=0}^{M-1} T_i(\tilde{\alpha}_n) T_j(\tilde{\tau}_n) \frac{\mathrm{d}T_k(\tilde{\zeta})}{\mathrm{d}\tilde{\zeta}} C_{\phi,ijk} \tag{3.14}$$

Integration was once more performed by fitting a Chebyshev polynomial to the integrand and integrating analytically. The function $f(\tilde{\alpha}, \tilde{\zeta})$ above was then determined by fitting a two-dimensional Chebyshev polynomial to the difference between the old representation of Φ and the integral. This essentially averaged out the problematic random noise in the τ-direction.

The integrated data and fitted f was then combined into a final Chebyshev polynomial representation of Φ in the domain. A final smoothing was applied by truncating the polynomial in the same manner as outlined in the previous section.

3.3.3. Combination of domains

With 16 sets of coefficients for the polynomials in the 16 domains, a single polynomial representation of Φ was then created for the whole region of interest. The naive implementation — a simple Chebyshev polynomial fit to selected points — gave poor representation of the derivatives of Φ. Therefore, a more advanced approach was developed.

$M^3 = 9^3 = 729$ evaluation points were chosen at Chebyshev nodes in $\tilde{\alpha}\tilde{\tau}\tilde{\zeta}$-space. For each point, Φ and its α_ℓ, τ, and ζ-derivatives were calculated and stored in the vectors $\mathbf{\Phi}$, $\mathbf{\Phi}_{\alpha_\ell}$, $\mathbf{\Phi}_\tau$, and $\mathbf{\Phi}_\zeta$. Then, three new matrices were defined: $\mathbf{A}_\alpha$, $\mathbf{A}_\tau$, and $\mathbf{A}_\zeta$. They are the three analytical derivatives of the original $\mathbf{A}$-matrix defined in equation 3.3.

The final Chebyshev coefficients $\boldsymbol{c}_{fin}$ for Φ were then given by a weighted least squares fit:

$$\boldsymbol{c}_{fin} = (\mathbf{X}^\mathsf{T}\mathbf{X})^{-1}\mathbf{X}^\mathsf{T}\boldsymbol{y} \ , \tag{3.15}$$

where

$$\mathbf{X} = \begin{bmatrix} 13\ \mathrm{diag}(\boldsymbol{\rho}^* \circ \boldsymbol{\Theta} \circ \boldsymbol{\zeta} \circ (\boldsymbol{\tau} + 0.5) \oslash \boldsymbol{\alpha}_\ell)\mathbf{A} \\ \mathbf{A}_\alpha \\ 220\ \mathrm{diag}(\boldsymbol{\rho}^* \oslash (\boldsymbol{\alpha}_\ell + 1))\mathbf{A}_\tau \\ 20\ \mathrm{diag}(\boldsymbol{\rho}^* \circ \boldsymbol{\Theta} \circ \boldsymbol{\zeta}^2)\mathbf{A}_\zeta \end{bmatrix} \tag{3.16}$$

and

$$\boldsymbol{y} = \begin{bmatrix} 13\ \boldsymbol{\rho}^* \circ \boldsymbol{\Theta} \circ \boldsymbol{\zeta} \circ (\boldsymbol{\tau} + 0.5) \oslash \boldsymbol{\alpha}_\ell \circ \boldsymbol{\Phi} \\ \boldsymbol{\Phi}_{\alpha_\ell} \\ 220\ \boldsymbol{\rho}^* \oslash (\boldsymbol{\alpha}_\ell + 1) \circ \boldsymbol{\Phi}_\tau \\ 20\ \boldsymbol{\rho}^* \circ \boldsymbol{\Theta} \circ \boldsymbol{\zeta}^2 \circ \boldsymbol{\Phi}_\zeta \end{bmatrix} . \tag{3.17}$$

The vectors $\boldsymbol{\rho}^*$, $\boldsymbol{\Theta}$, etc contain the values corresponding to each of the 729 points. The weights were adjusted by hand to give the best possible fit.

The coefficients were then truncated to 7th, 9th, and 7th order respectively to yield the final expression for Φ.

3.4. Equilibrium implementation

The new equation of state was implemented into my own thermochemical code EquiC, in order to optimise gas parameters and evaluate the EOS. EquiC has previously used BKW, JCZ3, and HMSA/C, and supports multiple condensed species. Since the scope of this work is limited to gases only, the program was modified to prevent the formation of solid and liquid products. This section gives a brief outline of the most fundamental parts of EquiC. The flowchart in figure 3.2 shows how the main functions are connected in the basic equilibrium loop.

The input data is prepared for the equilibrium solver by the preprocessor. It creates an array $\{n_i\}$ that contains the number of moles of each species for exactly 1 kg of substance in total. The equilibrium composition is roughly estimated according to a few simple rules. Hydrogen combines with oxygen, fluorine and chlorine to form water, hydrogen fluoride and hydrogen chloride, in that priority order. Carbon combines with oxygen to first form carbon monoxide and then carbon dioxide if additional oxygen is available. Nitrogen forms nitrogen gas. Any excess hydrogen, oxygen, chlorine or fluorine forms H_2, O_2, Cl_2 or F_2 respectively. The system volume V is the volume of 1 kg of matter. The enthalpy of formation of the compound or mixture (also for 1 kg) is used as a convenient approximation for the internal energy, which is then preserved in the system.

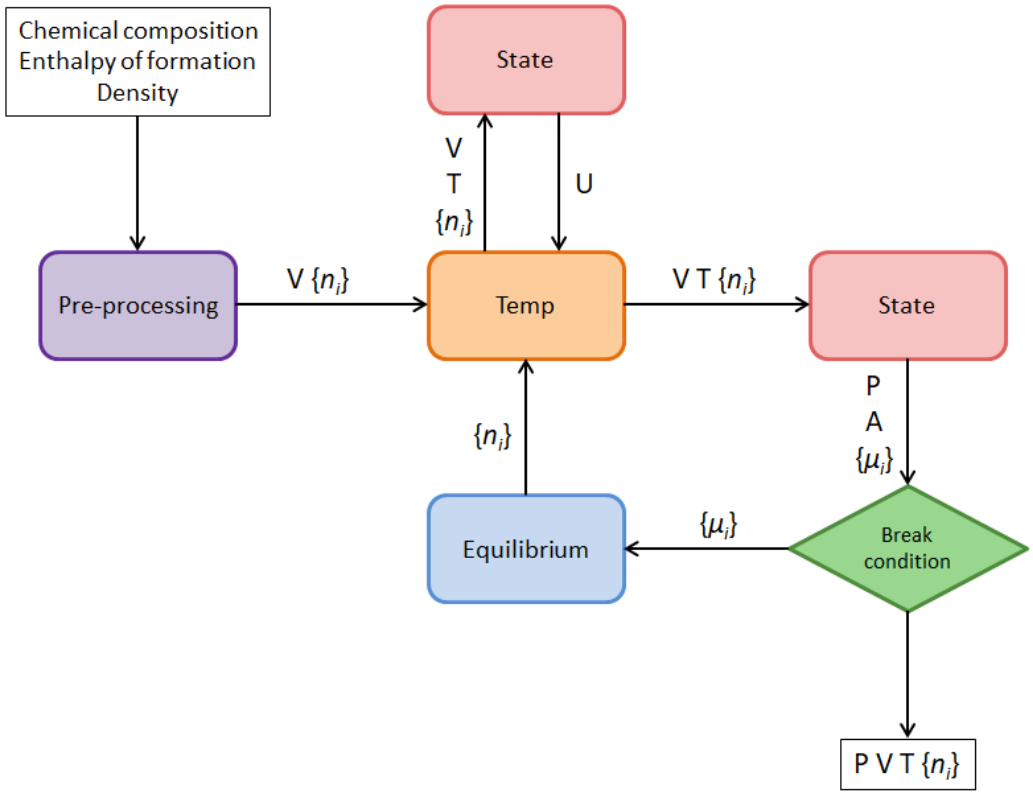

Figure 3.2. The basic equilibrium solving loop in EquiC.

The temperature solver (shown as "Temp" in the flowchart) takes the system volume, the chemical composition and the internal energy, and returns the temperature of the system. With no phase transitions, the internal energy is a nearly linear function of temperature. The default algorithm is Newton-Raphson, which converges in only three iterations. Each step uses the old temperature T_n to generate a new, better estimate T_{n+1}:

$$T_{n+1} = T_n - \frac{U - U_1}{c_V} \,. \tag{3.18}$$

Here, U is the current internal energy of the products which is calculated by the state function every iteration, and U_1 is the target internal energy. In a constant-volume combustion, it is equal to the internal energy of the unreacted substance. In the case of a shock wave or detonation, the shock energy has to be included as well (see equation 2.39). c_V is the constant-volume heat capacity.

The state function, shown as red boxes in figure 3.2, implements the excess free energy expression and its derivatives as outlined in sections 2.3 and 2.4. The ideal gas components of the entropy and internal energy are taken from JANAF Thermochemical Tables [38] and are stored in arrays with data points every 100 kelvin between 0 and 6000 K. Linear interpolation is used in between the data points, and the properties

are linearly extrapolated beyond 6000 K. Given a system volume, a temperature, and chemical composition array $\{n_i\}$, the function returns the thermodynamic properties of the system. This includes pressure, internal energy, free energy (A), entropy, and chemical potentials for all species ($\{\mu_i\}$).

The equilibrium solving function generates a better estimate of the chemical composition array $\{n_i\}$ in the system at current volume and temperature. The objective is to minimise the total Helmholtz free energy of the mixture. This is done by generating equilibrium constants for a number of hypothetical reactions, solving them sequentially, and updating the chemical composition. Compared to algorithms such as steepest descent, this method finds the global minimum and not just the closest local minimum.

The method requires at least one reaction for each product in the product library. The reactions are not necessarily reactions that would occur in reality, since equilibrium composition is unaffected by reaction path. The reactions were instead chosen to optimise convergence rate and numerical efficiency. A complete list is available in appendix B.

Consider the reaction a A + b B $\rightleftharpoons$ c C + d D. At chemical equilibrium, the dimensionless partial pressures of the products and reactants are related to the equilibrium constant K by the equation

$$K = \frac{p_C^c p_D^d}{p_A^a p_B^b} \,. \tag{3.19}$$

K is determined from the chemical potentials of the involved gases.

$$K = \exp\left(-\frac{c\mu_C + d\mu_D - a\mu_A - b\mu_B}{RT}\right) \tag{3.20}$$

By enforcing mass conservation, equation 3.19 is transformed into

$$(p_C + cx)^c (p_D + dx)^d - K(p_A - ax)^a (p_B - bx)^b = 0 \,, \tag{3.21}$$

which is solved for x, a variable that determines how much of each gas must be created or destroyed to achieve equilibrium. If $\min(a + b, c + d) \leq 2$, then equation 3.21 is solved analytically. Else, a second order Taylor series is expanded around $x = 0$ and solved to give an estimate of x which gradually converges each time the equilibrium function is called. After the equation has been solved once for every reaction, the $\{n_i\}$ vector is updated and returned.

A new temperature can then be calculated using the new composition array, and the loop continues until global equilibrium has been reached. This usually takes less than 50 iterations. This basic loop has been used to find the equilibrium state in both shock Hugoniots and detonations.

3.5. Determination of gas parameters

Several more or less complete exponential-6 product libraries are available in the literature [14], [20], [21], [39]. There are considerable differences between parameters in the different libraries, even for the most common gases. Therefore, the existing parameters of the most important species were evaluated and new parameters were optimised when necessary.

Shock Hugoniots provide a good test for an equation of state since extremely high pressures and densities are attainable. At several times liquid density and pressures in excess of a million atmospheres, the fluid is very far from an ideal gas, and as such its properties are very sensitive to the choice of exp-6 parameters. The states along the Hugoniot follows only a single line in pVT-space however, and initial testing revealed that experimental shock Hugoniot data could be adequately replicated by a range of different gas parameters. A high α (stiff molecule) could be compensated by a smaller r^* (radius). The potential well depth ε did not affect the fit considerably as long as it was within a fairly large interval. Therefore, an additional data source was required to properly evaluate and optimise parameters. Both Fried et al. [14] and Victorov et al. [20] used a combination of Hugoniot data and static pVT-measurements to calibrate their potential parameters. A similar approach was used in this work.

The NIST Chemistry WebBook [15] provides accurate reference equations of state for a long list of common fluids. Since they are based on essentially all available experimental data, they are expected to be more accurate than individual experimental data points. Another advantage is that properties are available at any point in pVT-space. Pressure, internal energy, heat capacity at constant volume (c_V) and speed of sound (c) were the four selected properties; the first two are first derivatives of the free energy and the last two are second derivatives. Their usual form is shown below [40].

$$c_V = \left(\frac{\partial U}{\partial T}\right)_\rho \tag{3.22}$$

$$c = \sqrt{\left(\frac{\partial p}{\partial \rho}\right)_S} \tag{3.23}$$

The cost function which was to be minimised during optimisation was constructed as a weighted sum of the relative errors. Shock pressure, shock velocity and particle velocity errors were given equal weights. For the static pVT-data, pressure was usually given weight 4, internal energy weight 2, and heat capacity and speed of sound each got weight 1. These two groups were normalised and usually given equal weight, however some gases required a much higher weight on the static properties in order to give the cost function a more sharply defined minimum. The optimisations were performed using exhaustive search.

The order of the parametrisation proved to be very important, since many gases could not be evaluated on their own. For example, monatomic nitrogen will always exist in an equilibrium with the much more stable diatomic nitrogen. N is only abundant enough to evaluate its exp-6 parameters under very strong shock compression of liquid nitrogen. The potential parameters for N_2 are required in order to simulate the shock compression, so they must be determined first. The workflow is outlined in the list below:

- N_2 was optimised using data from NIST and shock Hugoniot data below 40 GPa. The dissociation into N was negligible below this pressure.
- N constituted almost 2/3 of the shocked gas at 80 GPa, so the high pressure end of the Hugoniot was used to test parameters. Parameters from [14] gave a good fit.
- O_2 was tested using NIST and shock Hugoniot data. The parameters from [14] gave an excellent fit and required no further optimisation.
- O was more difficult to evaluate due to limited dissociation of O_2, but the values from [20] provided a good fit.
- H_2 was optimised using data from NIST and shock Hugoniots.
- H parameters from [14] then gave a good agreement with experimental shock temperature, pressure and velocity in the upper part of the Hugoniot.
- H_2O dissociates into H_2, O_2, H, and O when shocked to high pressures, but with these determined, the parameters for water could be optimised using shock data and static data from NIST.
- NH_3 was optimised in the same way as H_2O.
- CO and CO_2 are very important combustion products, but they break down into carbon when shocked to high pressures and could therefore not be optimised properly (since no condensed products are included). CO_2 parameters from [14] and [20] were evaluated at pressures below 40 GPa and those from [20] were slightly better. The CO parameters from [14] were chosen since they were closest to those of the isoelectronic and equally heavy N_2 molecule.
- NO_2, N_2O and NO were difficult to evaluate directly and parameters were taken from [20].
- CHNO and CH_2O_2 (hydrogen isocyanate and formic acid) are usually minor products but the choice of parameters proved to be important for the modelling of nitroesters. Parameters for CH_2O_2 in particular varied considerably in the literature but the most recent values from [21] were chosen. This gave excellent agreement with the experimental PETN Hugoniot in the 40–90 GPa region, where formic acid was predicted to be a major product.
- OH, the hydroxyl radical, was only available in the old JCZS library [11] and was

taken from there.

- Parameters for all other gases were taken from [14].

The complete product library is available in table A.1 in the appendix. Even if all these potential parameters would describe each gas perfectly on its own, there are still pair-interactions between different species which are not perfectly represented by the mixing rule (equation 2.4). Therefore, the equation contains k_{ij}, an unlike-pair correction factor for r^*_{ij}. Some previous works [21], [39] have included correction factors for ε_{ij} and α_{ij} as well, but these have often remained unused; probably because r^*_{ij} is the easiest one to calibrate.

Only four unlike-pair corrections were determined in this work. Since only a single value was adjusted for each case, and no advanced cost function was required, the optimisation was performed by hand. The values are listed in table A.2 in the appendix.

- N_2 – NH_3 was chosen to correctly reproduce the detonation velocity, pressure, and temperature of liquid hydrazoic acid. This explosive was predicted to produce mostly nitrogen and ammonia which makes it ideal for the calibration.
- N_2 – H_2O was adjusted to better predict the detonation velocity of hydrazoic acid/water mixtures. These produce almost exclusively N_2 and H_2O as products so no other species were expected to interfere.
- CH_2O_2 – N was calibrated using shock Hugoniot data for PETN above 90 GPa. Without a correction factor, the fit is good up to 90 GPa, after which the system becomes too soft. This coincides with the onset of dissociation of N_2 into N which cools the system, and rapidly increasing amount of CH_2O_2 which decreases the total amount of gas. Their unlike-pair constant was adjusted until the fit was good above 90 GPa as well.
- CO_2 – O has been given a correction factor by several authors, but since the best data source for evaluation is a high pressure CO_2 Hugoniot, the constant could not be optimised in this work. It was therefore taken from [14] instead.

Chapter 4.

Results

4.1. Evaluation of the Monte Carlo program

The Monte Carlo program was compared to reference simulations performed by Fried and Howard [19] in order to assess its accuracy. Nine state points with various densities, temperatures and stiffness coefficients were selected and Z and U^* calculated. 512 particles and 100 000 cycles were used in each simulation, compared to 1024 particles and 140 000 cycles in the reference calculations. The results are shown in the table below. The estimated standard error is denoted s. The 100 000 cycles were divided into 10 blocks of 10 000 cycles, each block long enough to be considered essentially independent from the others. The corrected sample standard deviation for the blocks was then divided by $\sqrt{10}$ to give the standard error s.

Table 4.1. The results of long Monte Carlo simulations compared to reference values. Estimated standard errors are denoted s.

State			512 particles, 100 000 cycles				Reference [19]			
ρ^*	T^*	α	Z	s_Z	U^*	s_U	Z_{ref}	s_Z	U^*_{ref}	s_U
3.8198	100	15.5	16.1730	0.0052	4.1189	0.0018	16.1734	0.0018	4.1193	0.0006
3.8198	100	13.5	9.9247	0.0010	2.8099	0.0004	9.9252	0.0007	2.8103	0.0003
3.8198	100	11.5	5.5030	0.0009	1.7974	0.0005	5.5049	0.0002	1.7982	0.0001
2.4749	20	15.5	15.9919	0.0065	2.8583	0.0018	15.9874	0.0020	2.8574	0.0006
2.4749	20	13.5	11.3064	0.0026	2.1600	0.0009	11.3049	0.0014	2.1596	0.0005
2.4749	20	11.5	7.3341	0.0016	1.4838	0.0007	7.3350	0.0005	1.4842	0.0002
1.4991	5	15.5	8.0751	0.0040	-0.1395	0.0009	8.0755	0.0018	-0.1387	0.0004
1.4991	5	13.5	6.5616	0.0046	-0.2677	0.0011	6.5626	0.0014	-0.2666	0.0003
1.4991	5	11.5	4.9173	0.0026	-0.4530	0.0008	4.9210	0.0011	-0.4515	0.0003

The results are overall extremely close to the reference. The differences and average absolute difference between the two sets are shown in table 4.2 below. The table also contains the t statistic from Welch's t-test, which is essentially how the difference compares to the combined standard errors. This was used to test the hypothesis that both Monte Carlo programs would converge on the same results given infinite computation

time. The largest (absolute) t is -1.97, which together with the approximately 9.6 degrees of freedom gives a two-tailed test p-value of 0.079. Without a more in-depth discussion about appropriate confidence intervals, the MC program written in this work probably converges slightly differently than the reference, but it cannot be definitely proved without more extensive simulations.

Table 4.2. The difference between present and reference calculations. The ratio of the differences and the combined standard errors are shown in the t-columns.

ρ^*	T^*	α	$Z - Z_{ref}$	t	$U^* - U^*_{ref}$	t
3.8198	100	15.5	-0.0004	-0.08	-0.0004	-0.19
3.8198	100	13.5	-0.0005	-0.41	-0.0004	-0.67
3.8198	100	11.5	-0.0019	-1.97	-0.0008	-1.41
2.4749	20	15.5	0.0045	0.67	0.0009	0.49
2.4749	20	13.5	0.0015	0.52	0.0004	0.35
2.4749	20	11.5	-0.0009	-0.51	-0.0004	-0.56
1.4991	5	15.5	-0.0004	-0.09	-0.0008	-0.86
1.4991	5	13.5	-0.0010	-0.22	-0.0011	-0.97
1.4991	5	11.5	-0.0037	-1.34	-0.0015	-1.77
Average			0.0017		0.0007	

As a comparison, the Z and U^* values from the fitted EOS are presented for the same nine state points in the table below. The estimated standard errors for 10 000 cycle long simulations are also shown. The average absolute differences are several times larger than those of the long MC simulations in the previous table but very close to the average standard errors. This indicates that the Monte Carlo implementation is not the main source of error, regardless of whether it converges exactly or not.

Table 4.3. The difference between the new EOS and reference values. The standard errors of 10 000-cycle MC calculations have been included as well.

ρ^*	T^*	α	Z_{EOS}	$Z_{EOS} - Z_{ref}$	s_Z	U^*_{EOS}	$U^*_{EOS} - U^*_{ref}$	s_U
3.8198	100	15.5	16.1649	-0.0085	0.0163	4.1196	0.0003	0.0057
3.8198	100	13.5	9.9285	0.0033	0.0032	2.8110	0.0007	0.0013
3.8198	100	11.5	5.4676	-0.0373	0.0030	1.7925	-0.0057	0.0017
2.4749	20	15.5	15.9823	-0.0051	0.0205	2.8530	-0.0044	0.0058
2.4749	20	13.5	11.3020	-0.0029	0.0082	2.1578	-0.0018	0.0029
2.4749	20	11.5	7.3178	-0.0172	0.0051	1.4848	0.0006	0.0023
1.4991	5	15.5	8.0742	-0.0013	0.0126	-0.1393	-0.0006	0.0027
1.4991	5	13.5	6.5531	-0.0095	0.0144	-0.2702	-0.0036	0.0034
1.4991	5	11.5	4.9150	-0.0060	0.0081	-0.4540	-0.0025	0.0026
Average				0.0101	0.0102		0.0022	0.0032

4.2. Representation of a simple exp-6 fluid

The extensive Monte Carlo simulations performed by Fried and Howard [19] have been used several times to benchmark statistical mechanical theories and equations of state over a wide range of conditions. The original set contains 57 data points, however two of the high density points fall outside the domain used in this work. In particular, one of them ($\rho^* = 5.8025$, $T^* = 100$, $\alpha = 15.5$) showed signs of freezing which makes it unsuitable for evaluating fluids. Gubin and Victorov excluded the same two points in their comparison [41].

Table 4.4 below shows the accuracy of a number of theories and equations of state. The first two are the statistical mechanical theories MCRSR and HMSA and the following four are polynomial representations used in various thermochemical codes. The improved KLRR uses around 40 000 coefficients [21], 4th order HMSA/C uses 1280 coefficients, 6th order HMSA/MC uses 4320 + 8 coefficients (the 8 being a correction polynomial) [19] and 5th order KLRR as used in Explo5 uses 125 coefficients, however with a much smaller valid region than the others [21]. The smoothed Monte Carlo results are the Chebyshev polynomials fitted to the Z and U data in the 16 domains, i.e. 32 polynomials with 4464 coefficients in total. The present EOS uses only 441 coefficients, a reduction by 90% with minimal loss of accuracy. It is several times more accurate than most other equations of state, and much less complicated than HMSA/MC which contains 20 separate domains and a correction polynomial based on the 57 Monte Carlo data points [19]. The average relative error of some set of values x_i compared to the reference values r_i is

$$\Delta x = \frac{1}{m} \sum_{i=1}^{m} \left| \frac{x_i - r_i}{r_i} \right| . \tag{4.1}$$

Table 4.4. Average relative errors of several equations of state compared to the reference MC data by Fried and Howard [19].

Method	Average relative error		Reference
	ΔZ (%)	ΔU (%)	
MCRSR	2.07	2.46	[41]
HMSA$^{(a)}$	0.69	1.65	[19]
Improved KLRR	0.60	0.87	[41]
HMSA/C 4th order	0.72	1.89	[41]
HMSA/MC 6th order$^{(a)}$	0.19	0.28	[19]
KLRR 5th order$^{(a)(b)}$	0.37	0.76	[21]
Smoothed MC results	0.11	0.25	This work
EOS	0.14	0.25	

$^{(a)}$ Evaluated using all 57 data points. $^{(b)}$ Valid over a smaller temperature range.

4.3. Representation of real gases

The excellent representation of an exp-6 fluid has little value if it cannot be used to model a real gas. The accuracy of the equation of state developed in this work has been tested for six gases: nitrogen, oxygen and hydrogen which are all nonpolar, roughly spherical molecules; carbon dioxide which is nonpolar but more elongated; and water and ammonia which are strongly polar molecules. Among these, the potential parameters for N_2, H_2, H_2O and NH_3 were optimised in this work. Four thermodynamic properties have been studied: pressure, internal energy, heat capacity and speed of sound. The calculated values have been compared to reference data from NIST Chemistry WebBook [15] over a wide range of conditions.

The fluid density at a given pressure is overall predicted very well by the model, with average deviation from the reference values on the order of 1%. The internal energy also showed excellent agreement for the nonpolar species, but a significant deviation for water and ammonia. In order to produce comparable error estimates for different gases, only the thermal energy was considered, i.e. the internal energy was set to 0 at absolute zero. The heat capacity and speed of sound are generally well predicted at high temperature, but the fits become gradually worse as the temperature drops and completely fail close to the critical temperature.

4.3.1. Nitrogen

Nitrogen data is available for the widest temperature and pressure range of all gases considered here. Five isotherms were calculated at temperatures of 300–2000 K and pressures between 0.2 and 2.2 GPa (2–22 kbar). They are shown in figure 4.1 together with reference data.

The average errors shown in table 4.5 are on the same order as the uncertainty of the reference values. While the error is evenly spread over the whole temperature range for the density and speed of sound c, the calculated heat capacity only shows significant deviation for the two lowest temperatures (300 and 600 K) and are well within experimental uncertainty elsewhere. Internal energy has a similar trend; the average deviation above 1000 K is less than 0.2%.

Table 4.5. Average relative errors of density, internal energy, heat capacity and speed of sound for nitrogen gas at 300–2000 K and 0.2–2.2 GPa. This is compared to the uncertainty of the reference values in the same region [15].

	Average relative error / uncertainty of NIST data			
	$\Delta\rho(\%)$	$\Delta U(\%)$	$\Delta c_V(\%)$	$\Delta c(\%)$
EOS	0.8	1.8	1.4	3.0
NIST data	0.6	-	>2	0.5–1.5

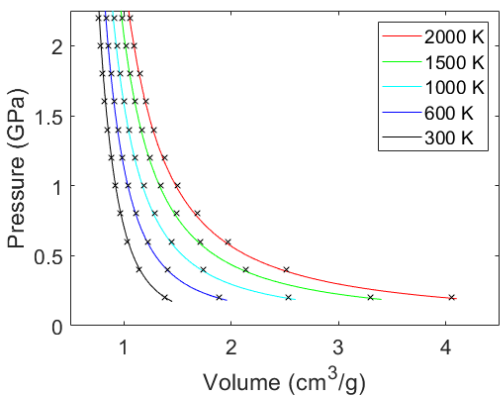

(a) Pressure vs specific volume.

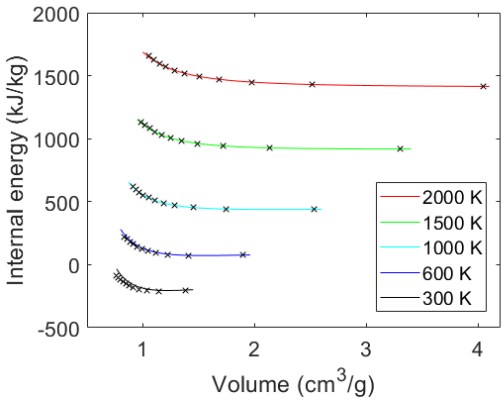

(b) Internal energy vs specific volume.

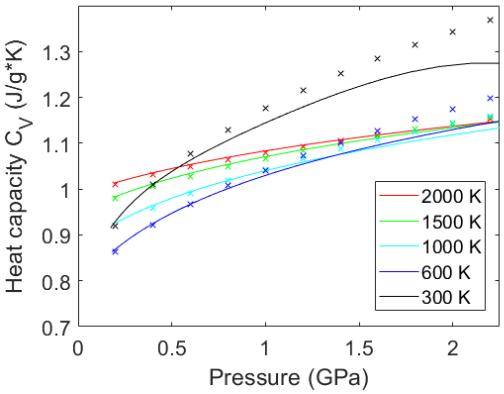

(c) Heat capacity vs pressure.

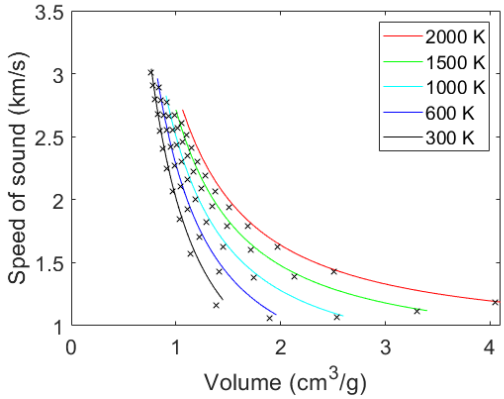

(d) Speed of sound vs specific volume.

Figure 4.1. Static properties of nitrogen gas. Solid lines are EOS isotherms and symbols are data from NIST [15]. The accuracy is overall very good but the heat capacity is underestimated at low temperature and high pressure.

4.3.2. Oxygen

Oxygen data was available in a much smaller pressure range, only up to 800 bar. Five isotherms were calculated in the 280–1000 K interval and three of them are shown in figure 4.2. The density error is similar to that of nitrogen, but the reference values have significantly lower uncertainty in this region. The mean speed of sound error is a considerable 14% at 280 K and pressures higher than 400 bar but quickly falls to 1% at 475 K and above, which is the same as the experimental uncertainty.

Table 4.6. Average relative errors of density, internal energy, heat capacity and speed of sound for oxygen gas at 280–1000 K and 20–80 MPa. This is compared to the uncertainty of the reference values in the same region [15].

	Average relative error / uncertainty of NIST data			
	$\Delta\rho(\%)$	$\Delta U(\%)$	$\Delta c_V(\%)$	$\Delta c(\%)$
EOS	0.8	0.4	0.8	3.0
NIST data	0.1	-	2	1

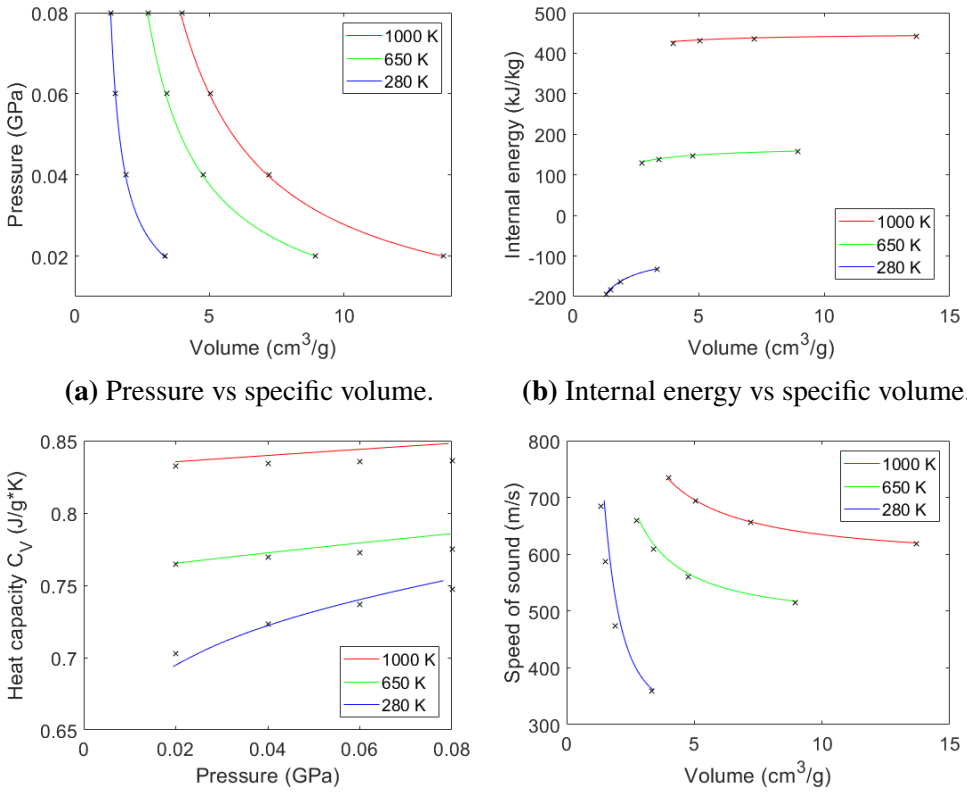

(a) Pressure vs specific volume.

(b) Internal energy vs specific volume.

(c) Heat capacity vs pressure.

(d) Speed of sound vs specific volume.

Figure 4.2. Static properties of oxygen gas. Solid lines are EOS isotherms and black symbols are data from NIST [15]. The fit is generally very good but the speed of sound is overestimated at low temperatures.

4.3.3. Hydrogen

Hydrogen data was available all the way up to 20 kbar and the error shows very much the same trends as for nitrogen and oxygen. Despite the good internal energy representation, there is a significant deviation in heat capacity, about 1.5% for the 1000 K isotherm and as much as 13% at 250 K and 2 GPa.

Table 4.7. Average relative errors of density, internal energy, heat capacity and speed of sound for hydrogen gas at 250–1000 K and 0.2–2 GPa. This is compared to the uncertainty of the reference values in the same region [42].

	Average relative error / uncertainty of NIST data			
	$\Delta\rho(\%)$	$\Delta U(\%)$	$\Delta c_V(\%)$	$\Delta c(\%)$
EOS	1.3	1.4	4.2	2.1
NIST data	1	-	1.0	-

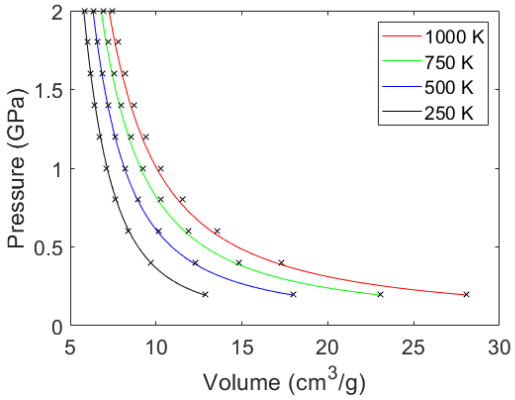

(a) Pressure vs specific volume.

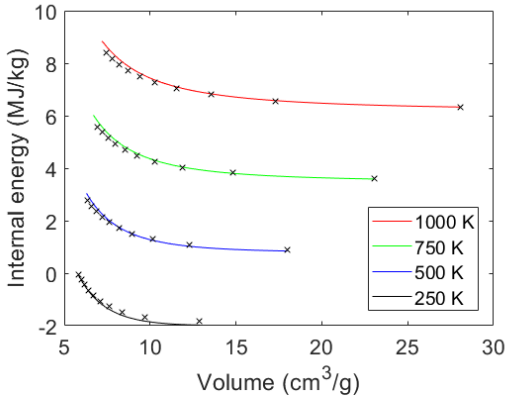

(b) Internal energy vs specific volume.

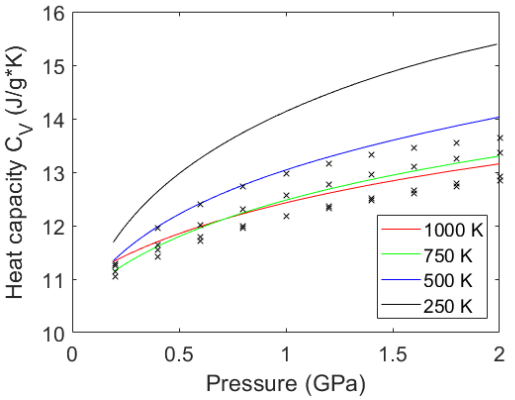

(c) Heat capacity vs pressure.

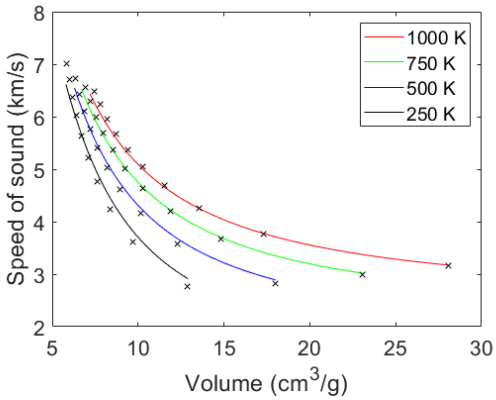

(d) Speed of sound vs specific volume.

Figure 4.3. Static properties of hydrogen gas. Solid lines are EOS isotherms and black symbols are data from NIST [15]. Heat capacity and speed of sound are not very well represented at low temperatures.

4.3.4. Carbon dioxide

The carbon dioxide fit has larger errors on average than the previous three gases. Density is still within experimental uncertainty, as is the speed of sound at high temperature and below 0.5 GPa, and the heat capacity above 800 kelvin. There is however a noticeable error in the internal energy which is carried over to the heat capacity at low temperature.

Table 4.8. Average relative errors of density, internal energy, heat capacity and speed of sound for carbon dioxide at 500–1100 K and 0.1–0.8 GPa. This is compared to the uncertainty of the reference values in the same region [43].

	Average relative error / uncertainty of NIST data			
	$\Delta\rho(\%)$	$\Delta U(\%)$	$\Delta c_V(\%)$	$\Delta c(\%)$
EOS	1.5	2.4	3.5	6.8
NIST data	1–2	-	2–4	1–4

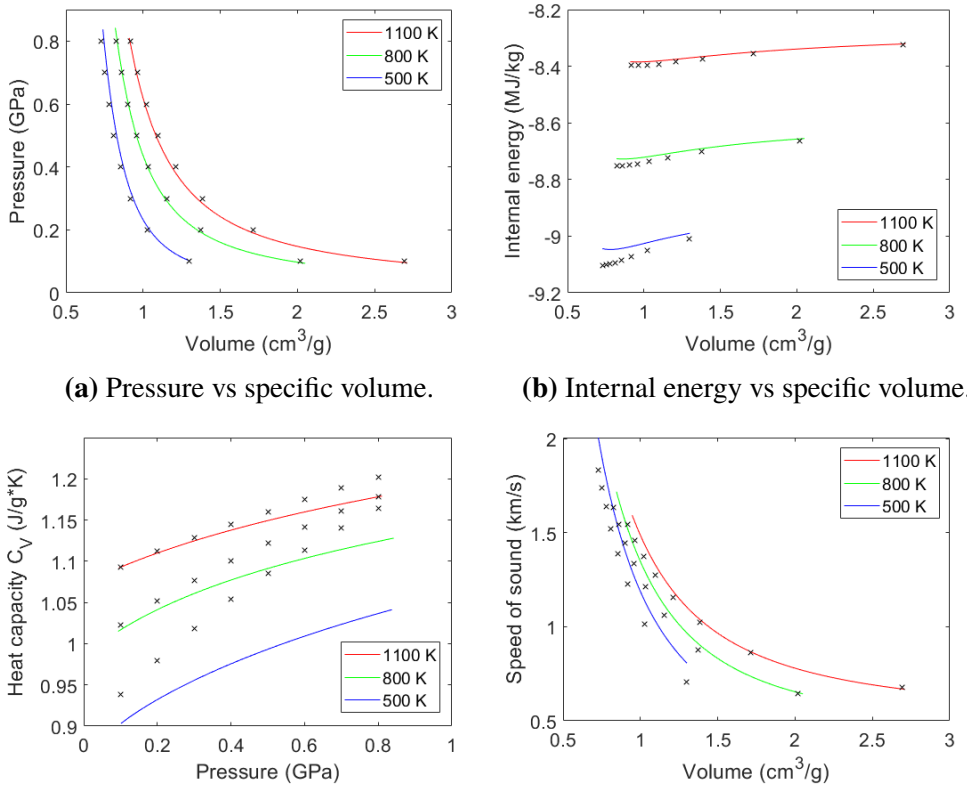

(a) Pressure vs specific volume.

(b) Internal energy vs specific volume.

(c) Heat capacity vs pressure.

(d) Speed of sound vs specific volume.

Figure 4.4. Static properties of carbon dioxide. Solid lines are EOS isotherms and black symbols are data from NIST [15]. Some deviation is seen for the internal energy which in turn leads to poorly represented heat capacity.

4.3.5. Water

The strongly polar water molecule is not nearly as well represented as the other gases. There is a near constant deviation in energy, which is noteworthy because the heat capacity is better represented despite being its derivative. The 700 K isotherm was extended down to ambient pressure in order to show the sharp peak in heat capacity close to the critical point (647 K and 22 MPa [15]); this is not captured at all by the EOS. The huge deviation in speed of sound at 700 K and 2 cm^3/g may be caused by numerical problems because it was very sensitive to step size.

Table 4.9. Average relative errors of density, internal energy, heat capacity and speed of sound for supercritical water at 700–1275 K and 0.1–1 GPa. This is compared to the uncertainty of the reference values in the same region [15].

	Average relative error / uncertainty of NIST data			
	$\Delta\rho(\%)$	$\Delta U(\%)$	$\Delta c_V(\%)$	$\Delta c(\%)$
EOS	1.4	9.2	6.7	13.7
NIST data	0.25–0.5	-	>0.5	-

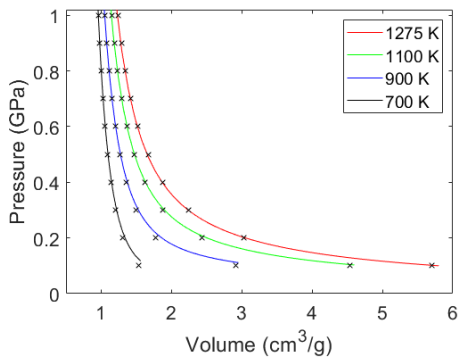

(a) Pressure vs specific volume.

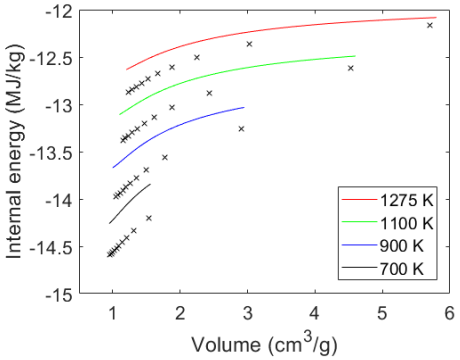

(b) Internal energy vs specific volume.

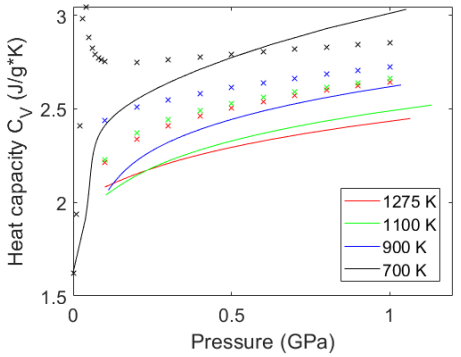

(c) Heat capacity vs pressure.

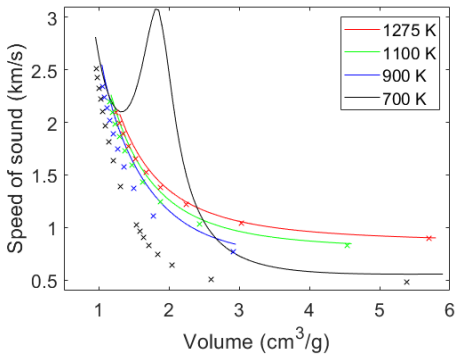

(d) Speed of sound vs specific volume.

Figure 4.5. Static properties of supercritical water. Solid lines are EOS isotherms and symbols are data from NIST [15].

4.3.6. Ammonia

Ammonia is also a polar molecule and the calculated isotherms deviated from the reference values in a similar way, but less severely. The exception was the density which had the best fit of all six gases. Another noteworthy observation is that the speed of sound is predicted more accurately at high pressure than moderate pressures.

Table 4.10. Average relative errors of density, internal energy, heat capacity and speed of sound for gaseous ammonia at 500–700 K and 0.1–1 GPa. This is compared to the uncertainty of the reference values in the same region [15].

	Average relative error / uncertainty of NIST data			
	$\Delta\rho(\%)$	$\Delta U(\%)$	$\Delta c_V(\%)$	$\Delta c(\%)$
EOS	0.5	5.8	3.5	7.1
NIST data	0.2	-	2	2

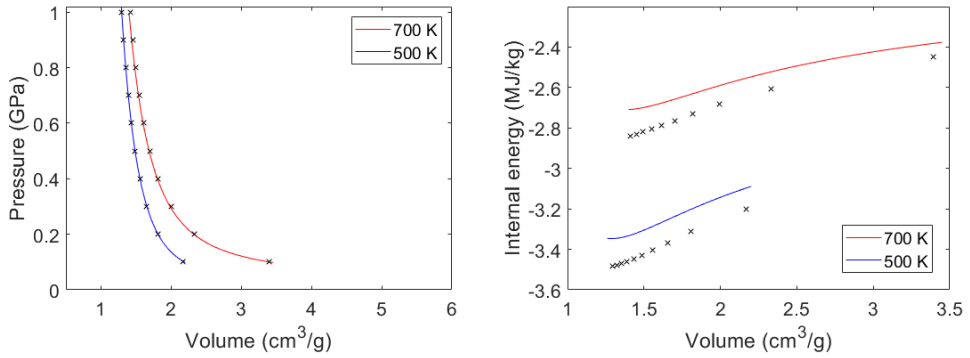

(a) Pressure vs specific volume. **(b)** Internal energy vs specific volume.

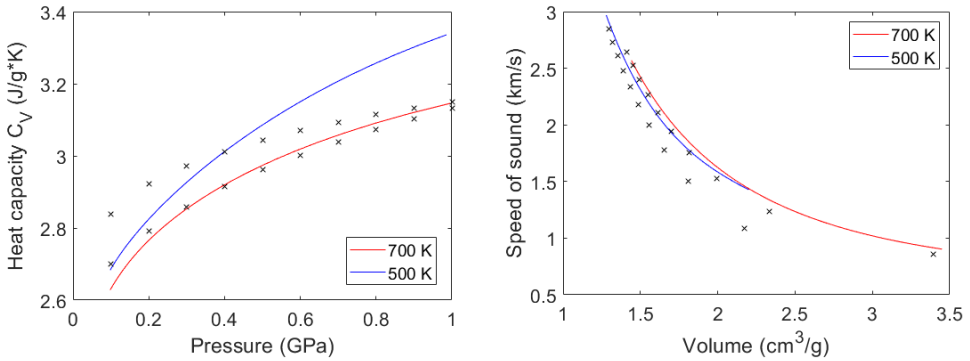

(c) Heat capacity vs pressure. **(d)** Speed of sound vs specific volume.

Figure 4.6. Static properties of gaseous ammonia. Solid lines are EOS isotherms and black symbols are data from NIST [15].

4.4. Shock Hugoniots

Experimental shock Hugoniot data served as a good test for gas parameters and the equation of state at more extreme conditions. The same six species were evaluated: N_2, O_2, H_2, CO_2, H_2O and NH_3, all initially in liquid form but shocked well into the supercritical region. All six calculated shock Hugoniots display excellent agreement with the experimental data. There is no noticeable difference in accuracy between polar and nonpolar molecules which indicates that the dipole approximation works well at elevated temperatures. The results for nitrogen and water are presented in figures 4.7 and 4.8 in this section; the rest which all look very similar are available in appendix C.

4.4.1. Nitrogen

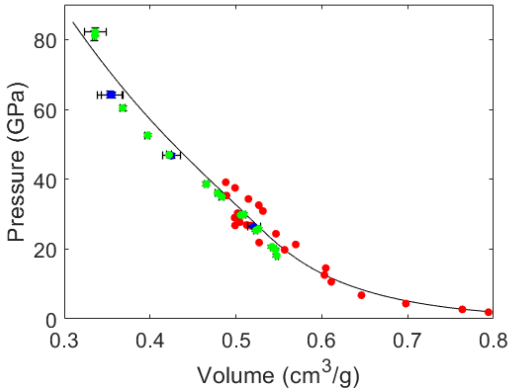

(a) Shock pressure as function of specific volume.

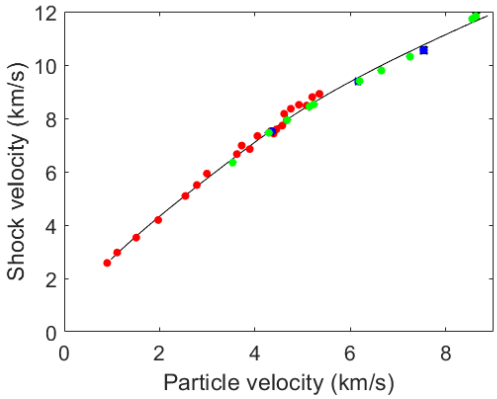

(b) Shock velocity as function of mass velocity.

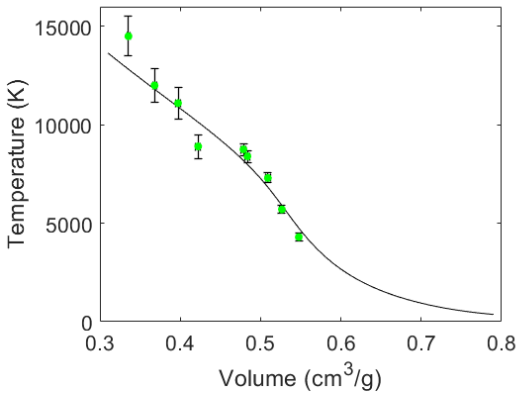

(c) Temperature as function specific volume.

Figure 4.7. Liquid nitrogen shock Hugoniot. The calculated values are shown as black lines, compared to experimental data from [30] (red), [31] (green) and [44] (blue).

The most prominent feature of the nitrogen Hugoniot, which is not seen as clearly for the other gases, is the sudden change of slope in the shock velocity/particle velocity plot. This marks the onset of the highly endothermic dissociation into monatomic nitrogen. The endothermic nature is clearly shown in subfigure 4.7 (c) as a change of slope around 0.5 cm^3/g. The experimental temperature seems to display a more complicated relationship with the shock volume than the calculated temperature, but it is hard to draw more exact conclusions due to the large experimental uncertainties.

4.4.2. Water

The water Hugoniot has a more standard shape with a nearly straight shock velocity–particle velocity relationship. The calculated curves pass within nearly all error bars, except for the temperature curve that is very slightly too high.

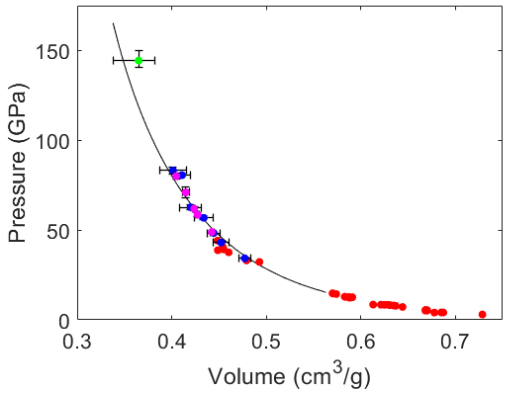

(a) Shock pressure as function of specific volume.

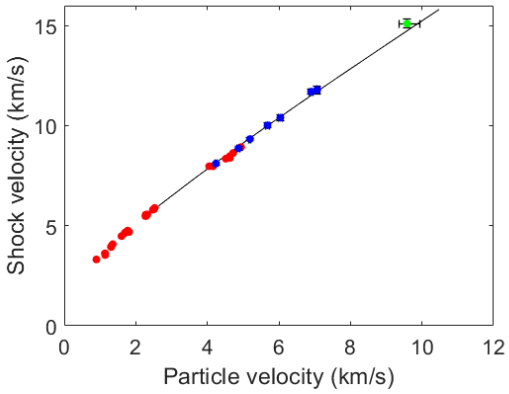

(b) Shock velocity as function of mass velocity.

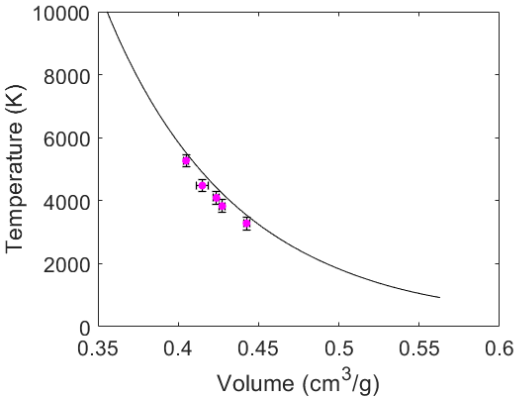

(c) Temperature as function specific volume.

Figure 4.8. Liquid water shock Hugoniot. The calculated values are shown as black lines, compared to experimental data from [30] (red), [45] (blue), [32] (green) and [46] (magenta).

The low-pressure tail of the Hugoniot could not be calculated. The low temperature (only slightly above critical temperature) and relatively high density (almost twice the normal liquid density) cause these states to fall outside the domain used in this work.

4.4.3. PETN

Pentaerytrhitol tetranitrate (PETN) is a high explosive on its own and has a well-defined detonation velocity and detonation pressure. It can also be shocked to higher pressures by external means, a phenomenon known as an overdriven detonation. Figure 4.9 shows the experimental overdriven shock Hugoniot of PETN compared to simulation results. The red and blue curves are from [14], calculated using HMSA/MC and JCZS respectively. The present model is shown as a black line. It was calculated based on the assumption that no carbon forms in the shock wave. PETN is very slightly oxygen deficient, so if carbon is formed, it is a minor product.

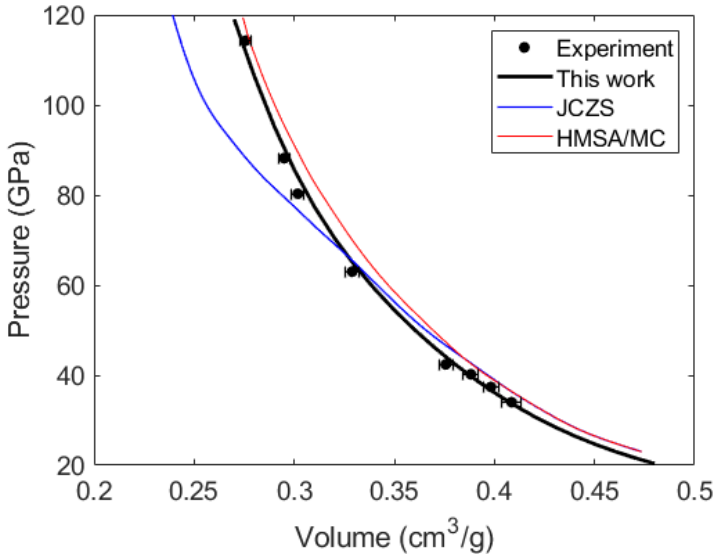

Figure 4.9. The calculated shock Hugoniot of PETN compared to experiments and two other models: HMSA/MC with the EXP6 library and the JCZS library [14]. The experiments were performed by Green et al. [47].

4.5. Detonations

The calculated C-J point in high explosives is very sensitive to the equation of state and gas parameters. Experimentally determined detonation velocities are also readily available in the literature. Table 4.11 lists ten different explosives: two slightly oxygen-positive nitrate esters, five hydrogen-free compounds, and three carbon-free explosives or mixtures. None of them are expected to form solid or liquid carbon so they can be modeled without a condensed phase equation of state. The table presents experimental detonation velocity (D), and when available, detonation pressure (P) and temperature as well. In addition to values calculated by EquiC, results from other thermochemical codes were included for comparison when available.

Table 4.11. Experimental and calculated detonation properties of ten different explosives.

Compound	ρ (g/cm^3)	D (km/s)	P (GPa)	T (K)	Method
Erythritol tetranitrate	1.702	7.97 ± 0.02			Experiment [48]
(ETN)		8.113			Cheetah [48]
$C_4H_6N_4O_{12}$		7.991	26.0	4184	EquiC
Nitroglycerin (NG)	1.6	7.70	25.3	4300 ± 100	Experiment [7]
$C_3H_5N_3O_9$		7.622	22.7	4372	EquiC
Liquid nitric oxide	1.3	5.62 ± 0.07	10 ± 1		Experiment [20]
NO		5.55	9.52	2858	TDS [20]
		5.552	9.5	2869	Explo5 [21]
		5.578	9.65	2868	EquiC
Tetranitromethane	1.65	6.45	15.5		Experiment [20]
(TNM)		6.46	15.0	2231	TDS [20]
CN_4O_8		6.45	14.9	2239	Explo5 [21]
		6.474	15.2	2246	EquiC
Hexanitroethane	1.86	7.58			Experiment [20]
(HNE)		7.58	23.8	2527	TDS [20]
$C_2N_6O_{12}$		7.584	23.7	2536	Explo5 [21]
		7.570	24.0	2531	EquiC
Hexanitrobenzene	1.973	9.33			Experiment [20]
(HNB)		9.34	39.0	4896	TDS [20]
$C_6N_6O_{12}$		9.313	38.5	4871	Explo5 [21]
		9.354	39.1	5058	EquiC
4,4'-Dinitro-3,3'	1.77	9.00 ± 0.10			Experiment [20]
-diazenofuroxan		8.94	33.3	5541	TDS [20]
(DDF)		8.915	33.0	5510	Explo5 [21]
$C_4N_8O_8$		8.995	33.6	5725	EquiC
Hydrazoic acid	1.127	7.57 ± 0.02	16.6	4710 ± 120	Experiment [49]
HN_3		7.572	16.4	4745	EquiC
Hydrazine nitrate (HN)	1.64	8.80 ± 0.05	21.1 ± 0.4		Experiment [50]
$H_5N_3O_3$		8.952	29.6	2226	EquiC
RX-23-AB	1.38	7.48 ± 0.07	18.5 ± 0.5		Experiment [26]
70% HN, 24.1% water,		7.763	17.9	2168	EquiC
5.9% hydrazine					

The majority of the calculations have excellent accuracy. The detonation velocity of the hydrogen-free explosives in particular deviate by 20 m/s on average and 42 m/s at most, well within the available experimental uncertainties. TDS and Explo5 are almost as accurate on average, but less consistent. Both programs underestimate DDF and liquid NO; the predictions of the latter are just at the lower bound of the experimental uncertainty.

The calculated values for ETN are in excellent agreement with recent experiments, both at high and low loading densities as shown in figure 4.10. NG is slightly underestimated in terms of detonation velocity (1%) and pressure (10 %). Those specific measurements lack reported uncertainties, but the authors note that "Detonation velocities can typically be measured to within a few percent" and "detonation pressures determined by various indirect methods span a range of 10–20%" [7].

The only cases for which the new EOS clearly fails are the carbon-free explosives that produce almost exclusively nitrogen and water as products. The detonation velocities of both HN and RX-23-AB are significantly overestimated. Hydrazoic acid-water mixtures also show significant deviations between simulations and experiments, see figure 4.11. A small fraction of water leads to high temperatures (over 3000 K) and the detonation velocity is underestimated in this region. As the water content approaches 50% by weight, the temperature falls below 2000 K and D is overestimated instead.

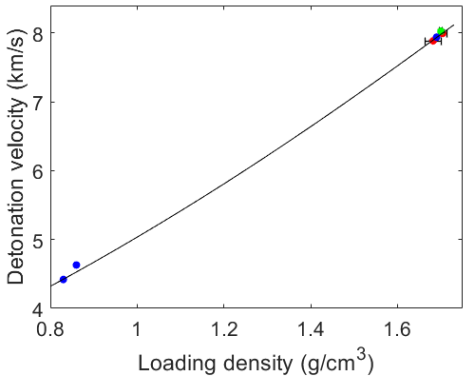

Figure 4.10. Detonation velocity of ETN at different densities. Simulation vs. experiments from [51] (blue), [52] (green), and [48] (red).

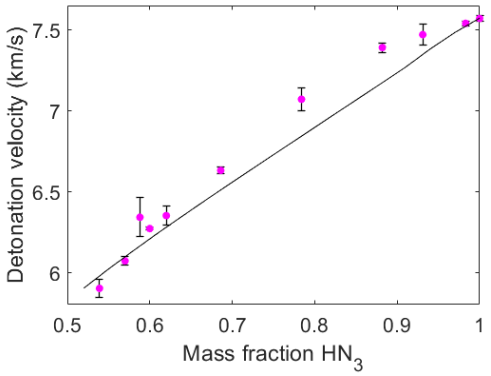

Figure 4.11. Detonation velocity of aqueous hydrazoic acid solutions. Simulation compared to experiments from [49].

Chapter 5.

Discussion

The equation of state developed in this work is a significant improvement in terms of both accuracy and simplicity when compared to other similar equations of state. When it comes to the representation of a simple exp-6 fluid, the small error can be attributed mainly to the uncertainty of the Monte Carlo simulations. Therefore, the accuracy of the EOS can be increased simply by running longer simulations. The computational cost is considerable even for marginal accuracy gains however. Halving the error requires four times longer simulations, and reducing it by a factor of ten would require a hundred times more computational power, on the order of 100 000 core-hours.

It is doubtful whether further improvements in the representation of a simple exp-6 fluid would improve its accuracy much more in practical applications. The limiting factor now seems to be the applicability of the exp-6 potential itself. The optimised gas parameters for nonpolar species have consistently reproduced the density and internal energy to about 1% and less than 2% respectively, compared to 0.14% and 0.25% for the simple exp-6 fluid. These are still excellent results considering that the uncertainties of the experimental data have been on the order of 1%.

The present EOS has shown its value in my thermochemical code. The implementation was straightforward and its polynomial form was numerically efficient as expected. Calculated detonation properties served as a good test for the equation of state and gas parameters, since the results are very sensitive to pressure, internal energy and the chemical potential of all species. The calculated detonation properties compare favourably with results from other thermochemical codes and seem to be slightly more accurate, at least for this selection of explosives. Only the explosives consisting of hydrogen, nitrogen and oxygen showed a significant deviation from the measured performance. The source of this deviation will be discussed in detail later in this section.

The most obvious shortcoming of this equation of state is caused by the underlying intermolecular potential. The spherically symmetric nature of exponential-6 cannot capture the complex interactions in polar liquids like water. Ree concluded that the potential of water can be approximated as spherically symmetric above 1300 K [25]. Indeed, the dipole approximation (equation 2.2) seems to work perfectly at elevated temperatures considering the excellent Hugoniot fit in figure 4.8. The dipole

approximation was not sufficient at lower temperatures; this was clearly shown by the poor representation of internal energy, heat capacity and speed of sound in the 700–1275 K range (figure 4.5). The internal energy deviation is interesting because it is consistently overestimated and nearly constant for respective isotherm. It is most likely caused by hydrogen bonding networks — more bonds in the fluid lowers its internal energy.

Fried et al. used an elegant solution to this problem: a multi-species model of polar molecules [14]. Water was represented by associated and non-associated water, treated as two separate species with the same chemical formula. Associated water had slightly smaller radius, lower internal energy and lower entropy, as would be expected when hydrogen bonds are prevalent. It was favoured at low temperature and high density, while regular non-associated dominated at high temperature. This allowed them to reproduce the low-pressure tail of the water Hugoniot, where a one-species model fails due to high density and low temperature. Smaller molecular radius leads to lower dimensionless density, and a lower internal energy leads to higher shock temperature. Both effects contribute to bringing the states into the domain of the equation of state. Fried et al. did not investigate the static internal energy, but the approach could most likely be used to correct that deviation as well.

The slightly overestimated shock temperature of water in the 50–80 GPa range is not necessarily caused by the equation of state however, but can probably be attributed to the product library. Several radicals are included, for example OH, H and O; but no ions like H^+, H_3O^+ and OH^-. Experiments have shown that significant ionisation occurs above 20 GPa based on the high electrical conductivity of shocked water [45]. This dissociation is endothermic, and could possibly explain the temperature difference.

The van der Waals one-fluid (vdW1f) mixing rules have been an incredibly fundamental assumption in this work. They allow the Monte Carlo results, which are based on identical exp-6 particles, to be applied to mixtures of gases with vastly different properties. The Lorentz-Berthelot rule similarly allowed the huge number of potential parameters for unlike-pair interactions to be approximated from pure gas parameters. Overall, the vdW1f and Lorentz-Berthelot rules have been remarkably successful considering their simplicity and empirical nature. There are however two important limitations, one related to the single-phase assumption and one related to the mixing rule itself.

All calculations in this work assumed a single, homogeneous mixture of all fluid components. This is a fair assumption, since gases are usually miscible. One pair of common gases is an important exception however — supercritical water and nitrogen undergo phase separation at elevated pressure. Costantino and Rice determined the solubility line experimentally up to 830 K, where phase separation occurs above 2.1 GPa [53]. No direct measurements are available at the extreme conditions in a detonation, but van Thiel and Ree simulated the phase separation in detonating RX-23-AB using the exp-6 potential [26]. Increasing k_{ij} for the H_2O-N_2 interaction to 1.04 was sufficient to cause phase separation at 2600 K and 18 GPa, which brought the calculated detonation velocity down much closer to the measured value. The only cases where detonation

velocities calculated by EquiC deviated significantly from experiment were hydrazine nitrate, RX-23-AB and aqueous solutions of hydrazoic acid. All three form almost exclusively nitrogen and water as products and the deviations are in line with the results from van Thiel and Ree. HN, RX-23-AB and dilute HN_3 solution are all overestimated by EquiC and have detonation temperatures around 2000 K. Phase separation would soften the system and lower detonation velocity. Concentrated HN_3 solutions on the other hand were underestimated by about 200 m/s and reach temperatures higher than 3000 K. This is in the single-phase region where an increased k_{ij} leads to a stiffer system and higher detonation velocity; setting k_{ij} to 1.05 indeed gave much better agreement with experiments.

The vdW1f mixing rules also have limited applicability to mixtures of gases with very dissimilar potential well depths. Bogdanova et al. determined that two species with an ε-ratio larger than 3 are poorly represented as an effective one-fluid, and showed that a two-component model based on perturbation theory could replicate Monte Carlo simulations much more successfully [54]. The problem has not been directly observed in this work. The similar ε-values of hydrogen-free detonation products may on the other hand be a reason behind the excellent results for this class of explosives.

The calibration of gas parameters was straightforward for common species like water, nitrogen, and oxygen but turned out to problematic for unstable species or more complicated molecules. Monatomic nitrogen, oxygen and hydrogen could still be validated through liquid shock Hugoniots of the respective species, since those were essentially two-component systems and parameters for the diatomic molecules were already known. The hydroxyl radical is an example of an even more difficult species. H_2O, H_2, O_2, H, and O will always be present in a system containing OH, and to determine potential parameters of a minor species in a six-component mixture is unfeasible due to the many sources of error. The parameters for OH used in this work are taken from the JCZS library, which in turn adopted parameters from old Lennard-Jones libraries.

It is easy to question the necessity of including minor species with uncertain parameters in the product library. However, it quickly became apparent that minor products play important roles in very specific cases. For example, the choice of parameters for formic acid and hydrogen isocyanate had a profound effect on the C-J point of PETN. The effect was not due to a direct change of pressure and temperature, but due to large changes in the equilibrium composition. Similarly, k_{ij} which corrects the unlike-pair parameters given by the Lorentz-Berthelot rule seemed to mostly affect the chemical equilibrium in multi-component mixtures, which made them hard to calibrate. Accurate experimental data for high-density binary mixtures are required to properly calibrate these constants. Again, it only works for stable products such as water and nitrogen (produced by RX-23-AB) or nitrogen and carbon dioxide (from hexanitrobenzene). The $CO_2 - O$ and $CH_2O_2 - N$ interactions are based on multi-component systems and are most likely less accurate.

Chapter 6.

Conclusions

In this thesis, I have developed a new equation of state for gases and supercritical fluids in the form of an analytical expression of the excess Helmholtz free energy. The idea of an analytical, numerically efficient EOS for use in chemical equilibrium calculations is not new. The two breakthroughs in this work have instead been the new variable transformation and the use of Monte Carlo simulations to generate the EOS. The new transformation has eliminated the need for multiple domains which reduced the number of polynomial coefficients tenfold. The inherently noisy Monte Carlo data has required a more complicated scheme in order to calculate the free energy and fit a polynomial expression, but the finished EOS is, to my knowledge, more accurate than any previous exponential-6 equation of state.

The EOS has been very successful in the representation of real gases. Small, nonpolar molecules are well modelled by the exponential-6 potential and their predicted thermodynamic properties have had excellent agreement with experimental data, from normal conditions up to 15000 K and a million times atmospheric pressure. Dense mixtures of detonation products are also well represented and the EOS can be used to accurately model shock and detonation phenomena. However, polar fluids and water in particular have not been adequately represented below 1300 K. A multi-species model of polar fluids is an interesting future extension to the equation of state.

There is also clearly a need for accurately determined potential parameters for radicals and other species that are difficult to isolate. Likewise, the Lorentz-Berthelot combination rules are not perfect but the lack of suitable experimental data makes the calibration very difficult. It is therefore worth investigating a more theoretical approach to this problem in the future. For example, the exact pair interaction between two molecules (same or different species) could be calculated using ab initio methods, rotationally averaged and finally fitted as exp-6 parameters. Such an approach could, if successful, greatly simplify the process of fitting potential parameters and allow the equation of state to be extended to any desired chemical system.

Bibliography

[1] R. Boyle, *A Defence of the Doctrine Touching the Spring and Weight of the Air,* ... London: Printed by F. G. for Thomas Robinson, 1662, pp. 57–60. [Online]. Available: https://bvpb.mcu.es/en/consulta/registro.cmd?id=406806.

[2] R. A. Borg, G. Kemister and D. A. Jones, "Chemical equilibrium calculations for detonation products", Defence Science and Technology Organization Canberra, Tech. Rep., 1995. [Online]. Available: https://apps.dtic.mil/sti/pdfs/ADA307323.pdf.

[3] N. Metropolis, A. W. Rosenbluth, M. N. Rosenbluth, A. H. Teller and E. Teller, "Equation of state calculations by fast computing machines", *The Journal of Chemical Physics*, vol. 21, no. 6, pp. 1087–1092, 1953. DOI: 10.1063/1.1699114.

[4] D. Frenkel, "Introduction to Monte Carlo methods", in *Computational Soft Matter: From Synthetic Polymers to Proteins*, N. Attig, K. Binder, H. Grubmüller and K. Kremer, Eds., John von Neumann Institute for Computing, vol. 23, NIC Series, 2004, pp. 29–60.

[5] C. L. Mader, "Fortran BKW: A code for computing the detonation properties of explosives", Los Alamos Scientific Laboratory, Tech. Rep., 1967. DOI: 10.2172/4307185.

[6] C. L. Mader, *Numerical Modeling of Explosives and Propellants*, 3rd ed. CRC Press, 2007, pp. 453–464, ISBN: 9781420052381.

[7] M. L. Hobbs and M. R. Baer, "Calibrating the BKW-EOS with a large product species data base and measured C-J properties", in *Proceedings Tenth International Detonation Symposium*, Office of Naval Research, 1993, pp. 409–418.

[8] L. E. Fried and P. Clark Souers, "BKWC: An empirical BKW parametrization based on cylinder test data", *Propellants, Explosives, Pyrotechnics*, vol. 21, no. 4, pp. 215–223, 1996. DOI: https://doi.org/10.1002/prep.19960210411.

[9] M. Suceska, S. Chan and A. How-Ghee, "Can the accuracy of BKW EOS be improved?", in *15th International Detonation Symposium, Proceedings*, Office of Naval Research, 2014. [Online]. Available: https://www.researchgate.net/publication/282865238_Can_the_Accuracy_of_BKW_EOS_be_Improved.

[10] M. Cowperthwaite and W. H. Zwisler, "The JCZ equations of state for detonation products and their incorporation into the tiger code", in *Proceedings 6th Symposium (International) on Detonation*, Office of Naval Research, 1976, pp. 162–170.

[11] B. C. McGee, M. L. Hobbs and M. R. Baer, "Exponential 6 parameterization for the JCZ3-EOS", Sandia National Laboratories, Tech. Rep., 1998. DOI: 10.2172/639774. [Online]. Available: https://www.osti.gov/biblio/639774.

[12] M. L. Hobbs, R. G. Schmitt and H. K. Moffat, "JCZS3 — an improved database for EOS calculations", Sandia National Laboratories, Tech. Rep., 2018. [Online]. Available: https://www.osti.gov/servlets/purl/1527248.

[13] J. M. Caillol, "Critical-point of the Lennard-Jones fluid: A finite-size scaling study", *The Journal of Chemical Physics*, vol. 109, no. 12, pp. 4885–4893, 1998. DOI: 10.1063/1.477099.

[14] L. E. Fried, W. M. Howard and P. C. Souers, "EXP6: A new equation of state library for high pressure thermochemistry", in *Proceedings of the 12th International Detonation Symposium*, Office of Naval Research, 2002, pp. 567–575.

[15] E. W. Lemmon, M. O. McLinden and D. G. Friend, "Thermophysical properties of fluid systems", in *NIST Chemistry WebBook, NIST Standard Reference Database Number 69*, P. Linstrom and W. Mallard, Eds. Gaithersburg MD, 20899: National Institute of Standards and Technology, [Accessed between 2020-11-11 and 2021-01-14]. DOI: https://doi.org/10.18434/T4D303.

[16] F. H. Ree, "A statistical mechanical theory of chemically reacting multiphase mixtures: Application to the detonation properties of PETN", *The Journal of Chemical Physics*, vol. 81, no. 3, pp. 1251–1263, 1984. DOI: 10.1063/1.447811.

[17] ——, "Simple mixing rule for mixtures with exp-6 interactions", *The Journal of Chemical Physics*, vol. 78, no. 1, 409–415, 1983. DOI: 10.1063/1.444517.

[18] W. B. Brown, "Analytical representation of the excess thermodynamic equation of state for classical fluid mixtures of molecules interacting with α-exponential-six pair potentials up to high densities", *The Journal of Chemical Physics*, vol. 87, no. 1, pp. 566–577, 1987. DOI: 10.1063/1.453605.

[19] L. E. Fried and W. M. Howard, "An accurate equation of state for the exponential-6 fluid applied to dense supercritical nitrogen", *The Journal of Chemical Physics*, vol. 109, no. 17, 7338–7348, 1998. DOI: 10.1063/1.476520.

[20] S. Victorov, H. El-Rabii, S. Gubin, I. Maklashova and Y. Bogdanova, "An accurate equation-of-state model for thermodynamic calculations of chemically reactive carbon-containing systems", *Journal of Energetic Materials*, vol. 28, pp. 35–49, Oct. 2010. DOI: 10.1080/07370652.2010.491496.

[21] M. Suceska, M. Braithwaite, T. M. Klapötke and B. Stimac, "Equation of state of detonation products based on exponential-6 potential model and analytical representation of the excess Helmholtz free energy", *Propellants, Explosives, Pyrotechnics*, vol. 44, no. 5, pp. 564–571, 2019. DOI: https://doi.org/10.1002/prep.201800339.

[22] N. Desbiens and V. Dubois, "New developments of the CARTE thermochemical code: II – evaluation of the accuracy of the KLRR perturbation theory and treatment of mixtures", *EPJ Web of Conferences*, vol. 10, no. 00013, 2010. DOI: 10.1051/epjconf/20101000013.

[23] P. Samuels, K. Spangler, D. Iwaniuk, R. Cornell, E. L. Baker and L. I. Stiel, "Detonation performance analyses for recent energetic molecules", *AIP Conference Proceedings*, vol. 1979, no. 1, 2018. DOI: 10.1063/1.5044989.

[24] H. L. Vörtler, I. Nezbeda and M. Lísal, "The exp-6 potential fluid at very high pressures: Computer simulations and theory", *Molecular Physics*, vol. 92, no. 5, pp. 813–824, 1997. DOI: 10.1080/002689797169763.

[25] F. H. Ree, "Molecular interaction of dense water at high temperature", *The Journal of Chemical Physics*, vol. 76, no. 12, pp. 6287–6302, 1982. DOI: 10.1063/1.443032.

[26] M. van Thiel and F. H. Ree, "Unlike pair interactions in N2-H2O mixtures", *AIP Conference Proceedings*, vol. 309, no. 1, pp. 81–84, 1994. DOI: 10.1063/1.46225.

[27] Y. Kataoka, "Equation of state of the fluid defined by the modified buckingham (exp-6) potential derived by molecular dynamics simulations", *Bulletin of the Chemical Society of Japan*, vol. 65, no. 8, pp. 2093–2103, 1992. DOI: 10.1246/bcsj.65.2093.

[28] D. E. Aspnes, "Digital data smoothing utilizing Chebyshev polynomials", *Analytical Chemistry*, vol. 47, no. 7, pp. 1181–1183, 1975. DOI: 10.1021/ac60357a035.

[29] G. W. Stewart, *Afternotes on Numerical Analysis*. Philadelphia, Pa: Society for Industrial and Applied Mathematics, 1996, pp. 150–153, ISBN: 9780898713626.

[30] S. P. Marsh, Ed., *LASL Shock Hugoniot Data*. University of California Press, 1980, ISBN: 0-520-04008-2.

[31] W. J. Nellis, H. B. Radousky, D. C. Hamilton, A. C. Mitchell, N. C. Holmes, K. B. Christianson and M. van Thiel, "Equation-of-state, shock-temperature, and electrical-conductivity data of dense fluid nitrogen in the region of the dissociative phase transition", *The Journal of Chemical Physics*, vol. 94, no. 3, pp. 2244–2257, 1991. DOI: 10.1063/1.459895.

[32] T. Kimura, N. Ozaki, T. Sano, T. Okuchi, T. Sano, K. Shimizu, K. Miyanishi, T. Terai, T. Kakeshita, Y. Sakawa and R. Kodama, "P-ρ-t measurements of H2O up to 260 GPa under laser-driven shock loading", *The Journal of Chemical Physics*, vol. 142, no. 16, 2015. DOI: 10.1063/1.4919052.

[33] C. L. Mader, *Numerical Modeling of Explosives and Propellants*, 3rd ed. CRC Press, 2007, pp. 1–4, ISBN: 9781420052381.

[34] E. de Miguel and G. Jackson, "The nature of the calculation of the pressure in molecular simulations of continuous models from volume perturbations", *The Journal of Chemical Physics*, vol. 125, no. 16, 2006. DOI: 10.1063/1.2363381.

[35] ISO/IEC, *Programming languages — C*, https://web.archive.org/web/20181230041359if_/http://www.open-std.org/jtc1/sc22/wg14/www/abq/c17_updated_proposed_fdis.pdf, [Online; accessed 2021-01-14].

[36] Wikipedia, *Mersenne Twister — Wikipedia, the free encyclopedia*, http://en.wikipedia.org/w/index.php?title=Mersenne%20Twister&oldid=990691870, [Online; accessed 2020-12-11], 2020.

[37] E. A. Sultanik, *The MTwister C Library*, 2014. [Online]. Available: https://github.com/ESultanik/mtwister.

[38] T. Allison, *JANAF thermochemical tables, NIST standard reference database 13*, 1996. DOI: 10.18434/T42S31. [Online]. Available: https://janaf.nist.gov/.

[39] V. Dubois, N. Desbiens and E. Auroux, "New developments of the carte thermochemical code: Calculation of detonation properties of high explosives", *Chemical Physics Letters*, vol. 494, no. 4, pp. 306 –311, 2010, ISSN: 0009-2614. DOI: https://doi.org/10.1016/j.cplett.2010.05.093.

[40] International Association for the Properties of Water and Steam, IAPWS R6-95(2018), "Revised release on the IAPWS formulation 1995 for the thermodynamic properties of ordinary water substance for general and scientific use", 2018. [Online]. Available: http://www.iapws.org/relguide/IAPWS95-2018.pdf.

[41] S. A. Gubin and S. B. Victorov, "The accuracy of the theories based on statistical physics for the thermodynamic modeling of state parameters of dense pure gases (fluids)", *Journal of Physics: Conference Series*, vol. 1205, 2019. DOI: 10.1088/1742-6596/1205/1/012020.

[42] J. W. Leachman, R. T Jacobsen, S. G. Penoncello and E. W. Lemmon, "Fundamental equations of state for parahydrogen, normal hydrogen, and orthohydrogen", *Journal of Physical and Chemical Reference Data*, vol. 38, no. 3, pp. 721–748, 2009. DOI: 10.1063/1.3160306.

[43] R. Span and W. Wagner, "A new equation of state for carbon dioxide covering the fluid region from the triple-point temperature to 1100 K at pressures up to 800 MPa", *Journal of Physical and Chemical Reference Data*, vol. 25, no. 6, pp. 1509–1596, 1996. DOI: 10.1063/1.555991.

[44] W. J. Nellis and A. C. Mitchell, "Shock compression of liquid argon, nitrogen, and oxygen to 90 GPa (900 kbar)", *The Journal of Chemical Physics*, vol. 73, no. 12, pp. 6137–6145, 1980. DOI: 10.1063/1.440105.

[45] A. C. Mitchell and W. J. Nellis, "Equation of state and electrical conductivity of water and ammonia shocked to the 100 GPa (1 Mbar) pressure range", *The Journal of Chemical Physics*, vol. 76, no. 12, pp. 6273–6281, 1982. DOI: 10.1063/1.443030.

[46] G. A. Lyzenga, T. J. Ahrens, W. J. Nellis and A. C. Mitchell, "The temperature of shock-compressed water", *The Journal of Chemical Physics*, vol. 76, no. 12, pp. 6282–6286, 1982. DOI: 10.1063/1.443031.

[47] L. Green, N. Holmes and J. Kury, "Shock measurements on explosives in the supra compressive region", in *International Symposium on Pyrotechnics and Explosives*, Beijing, China, 1987, pp. 692–698.

[48] V. W. Manner, D. N. Preston, B. C. Tappan, V. E. Sanders, G. W. Brown, E. Hartline and B. Jensen, "Explosive performance properties of erythritol tetranitrate (ETN)", *Propellants, Explosives, Pyrotechnics*, vol. 40, no. 4, pp. 460–462, 2015. DOI: https://doi.org/10.1002/prep.201500066.

[49] R. K. Kurbangalina, E. A. Patskov, L. N. Stesik and G. S. Yakovleva, "Detonation of liquid hydrazoic acid and its aqueous solutions", *Journal of Applied Mechanics and Technical Physics*, vol. 11, pp. 672–677, 1970.

[50] A. V. Utkin, V. M. Mochalova, S. I. Torunov, V. A. Sosikov, V. A. Garanin and L. B. Romanova, "Detonation properties of hydrazine nitrate", *Journal of Physics: Conference Series*, vol. 1147, 2019. DOI: 10.1088/1742-6596/1147/1/012034.

[51] R. Matyáš, M. Künzel, A. Růžička, P. Knotek and O. Vodochodský, "Explosive properties of erythritol tetranitrate", *Propellants, Explosives, Pyrotechnics*, vol. 35, 2013. DOI: 10.1002/prep.201300121.

[52] M. Künzel, R. Matyáš, O. Vodochodský and J. Pachman, "Explosive properties of melt cast erythritol tetranitrate (ETN)", *Central European Journal of Energetic Materials*, vol. 14, pp. 418–429, May 2017. DOI: 10.22211/cejem/68471.

[53] M. Costantino and S. F. Rice, "Supercritical phase separation in H2O-N2 mixtures", *Journal of Chemical Physics*, vol. 95, no. 23, 9034–9036, 1991. DOI: https://doi.org/10.1021/j100176a004.

[54] Y. A. Bogdanova, A. A. Anikeev, S. A. Gubin and S. B. Victorov, "Limits of the applicability of the effective one-fluid model", *Russian Journal of Physical Chemistry A*, vol. 89, no. 5, pp. 741–746, 2015. DOI: 10.1134/s003602441505009x.

[55] W. J. Nellis, A. C. Mitchell, M. van Thiel, G. J. Devine, R. J. Trainor and N. Brown, "Equation-of-state data for molecular hydrogen and deuterium at shock pressures in the range 2–76 GPa (20–760 kbar)", *The Journal of Chemical Physics*, vol. 79, no. 3, pp. 1480–1486, 1983. DOI: 10.1063/1.445938.

[56] T Sano, N Ozaki, T Sakaiya, K Shigemori, M Ikoma, T Kimura, K Miyanishi, T Endo, A Shiroshita, H Takahashi, T Jitsui, Y Hori, Y Hironaka, A Iwamoto, T Kadono, M Nakai, T Okuchi, K Otani, K Shimizu, T Kondo, R Kodama and K Mima, "Hugoniot and temperature measurements of liquid hydrogen by laser-shock compression", *Journal of Physics: Conference Series*, vol. 244, no. 4, 2010. DOI: 10.1088/1742-6596/244/4/042018.

[57] G. L. Schott, "Shock-compressed carbon dioxide: Liquid measurements and comparisons with selected models", *High Pressure Research*, vol. 6, no. 3, pp. 187–200, 1991. DOI: 10.1080/08957959108203209.

Appendix A.

Product library

Table A.1. The product library used in EquiC.

Product	Formula	r_m (Å)	ε/k_B (K)	α	λ (K)	Reference
Argon	Ar	4.07	86.1	13	0	[14]
Acetylene	C_2H_2	4.51	241.8	13.6	0	[14]
Ethylene	C_2H_4	4.67	196.2	12.2	0	[14]
Ethane	C_2H_6	4.84	238.5	13.9	0	[14]
Carbon tetrachloride	CCl_4	5.99	650.7	13.6	0	[14]
Carbonyl chloride fluoride	CClFO	5.07	300	13	0	[14]
Carbon tetrafluoride	CF_4	4.67	602.5	14.5	0	[14]
Trifluoromethyl hypofluorite	CF_3OF	4.86	200	13	0	[14]
Carbonyl fluoride	CFO	4.51	200	13	0	[14]
Dichloromethane	CH_2Cl_2	5.55	305.8	12.1	0	[14]
Difluoromethane	CH_2F_2	5.03	233	11.9	0	[14]
Formic acid	CH_2O_2	4.62	150	13	0	[21]
Methanol	CH_3OH	4.24	507.2	13	0	[14]
Methane	CH_4	4.3	137.8	12.3	0	[14]
Trichloromethane	$CHCl_3$	5.74	301	15.3	0	[14]
Formyl fluoride	CHFO	4.5	150	13	0	[14]
Hydrogen isocyanate	CHNO	4.8	232	13	0	[21]
Monatomic chlorine	Cl	3.9	130.9	13	0	[14]
Chlorine	Cl_2	4.93	346.7	11.3	0	[14]
Carbon monoxide	CO	4.16	105.5	13.2	0	[14]
Carbon dioxide	CO_2	4.22	230.2	13.8	0	[20]
Carbonyl chloride	COCl	4.92	250	13	0	[14]
Phosgene	$COCl_2$	5.25	368	13	0	[14]
Monatomic fluorine	F	3.33	113	13	0	[14]
Fluorine	F_2	3.8	92.2	13	0	[14]
Monatomic hydrogen	H	2.1	50	11	0	[14]
Hydrogen	H_2	3.62	33.2	10.94	0	This work
Water	H_2O	3.31	315	11.52	225	This work
Hydrogen chloride	HCl	3.84	198.4	13.9	0	[14]
Hydrogen cyanide	HCN	5.37	358.2	13.6	0	[14]
Helium	He	2.97	10.7	13	0	[14]
Hydrogen fluoride	HF	3.27	393.3	13.4	0	[14]
Monatomic nitrogen	N	2.43	88.2	11.4	0	[14]
Nitrogen	N_2	4.14	100.6	13.35	0	This work

Product	Formula	r_m (Å)	ε/k_B (K)	α	λ (K)	Reference
Nitrous oxide	N_2O	4.27	234.3	13.8	0	[20]
Ammonia	NH_3	3.718	229	12.08	112	This work
Nitric oxide	NO	3.7	140.2	13.9	0	[20]
Nitrogen dioxide	NO_2	4.27	326.2	13.8	0	[20]
Monatomic oxygen	O	2.57	277	11.5	0	[20]
Oxygen	O_2	3.83	121.2	13.6	0	[14]
Ozone	O_3	4.41	204.8	13.6	0	[14]
Hydroxyl	OH	3.29	80	13	0	[11]
Xenon	Xe	4.37	243.1	13	0	[14]

Table A.2. Unlike-pair corrections used in EquiC.

Interaction	k_{ij}	Reference
CO_2 - O	0.897	[14]
N_2 - NH_3	1.039	This work
N_2 - H_2O	1.01	This work
CH_2O_2 - N	1.07	This work

Appendix B.

Chemical reactions

Table B.1. List of all reactions that are considered in the equilibrium solver of EquiC.

$CH_4 + CO \longrightarrow C_2H_2 + H_2O$
$C_2H_2 + H_2 \longrightarrow C_2H_4$
$C_2H_4 + H_2 \longrightarrow C_2H_6$
$2\,CH_4 \longrightarrow C_2H_6 + H_2$
$CO_2 + 2\,Cl_2 \longrightarrow CCl_4 + O_2$
$COCl + F \longrightarrow CClFO$
$CO_2 + 2\,F_2 \longrightarrow CF_4 + O_2$
$2\,CF_4 + O_2 \longrightarrow 2\,CF_4O$
$2\,CO + F_2 \longrightarrow 2\,CFO$
$CO_2 + 2\,HCl \longrightarrow CH_2Cl_2 + O_2$
$CCl_4 + 2\,H_2 \longrightarrow CH_2Cl_2 + 2\,HCl$
$CO_2 + 2\,HF \longrightarrow CH_2F_2 + O_2$
$CF_4 + 2\,H_2 \longrightarrow CH_2F_2 + 2\,HF$
$CO + H_2O \longrightarrow CH_2O_2$
$CO_2 + H_2 \longrightarrow CH_2O_2$
$CH_2O_2 + H_2O \longrightarrow CH_3OH + O_2$
$CO_2 + 2\,H_2 \longrightarrow CH_4 + O_2$
$CCl_4 + HCl \longrightarrow CHCl_3 + Cl_2$
$H + CFO \longrightarrow CHFO$
$NH_3 + CO \longrightarrow CHNO + H_2$
$Cl_2 \longrightarrow 2\,Cl$
$2\,CO + O_2 \longrightarrow 2\,CO_2$
$CO + Cl \longrightarrow COCl$
$CO + Cl_2 \longrightarrow COCl_2$
$F_2 \longrightarrow 2\,F$
$H_2 \longrightarrow 2\,H$
$2\,H_2 + O_2 \longrightarrow 2\,H_2O$
$H_2 + 2\,OH \longrightarrow 2\,H_2O$
$H_2 + Cl_2 \longrightarrow 2\,HCl$
$CO + NH_3 \longrightarrow HCN + H_2O$
$H_2 + F_2 \longrightarrow 2\,HF$
$N_2 \longrightarrow 2\,N$

$$2\,N_2 + O_2 \longrightarrow 2\,N_2O$$
$$N_2 + 3\,H_2 \longrightarrow 2\,NH_3$$
$$N_2 + O_2 \longrightarrow 2\,NO$$
$$N_2 + 2\,O_2 \longrightarrow 2\,NO_2$$
$$O_2 \longrightarrow 2\,O$$
$$O_2 + O \longrightarrow O_3$$
$$O_2 + H_2 \longrightarrow 2\,OH$$
$$CO + H_2O \longrightarrow CO_2 + H_2$$
$$CO_2 + NH_3 \longrightarrow CHNO + H_2O$$
$$2\,CHNO \longrightarrow C_2H_2 + 2\,NO$$
$$C_2H_2 + N_2 \longrightarrow 2\,HCN$$
$$C_2H_2 + 2\,O_2 \longrightarrow 2\,CO_2 + H_2$$

Appendix C.

Additional shock Hugoniots

C.1. Oxygen

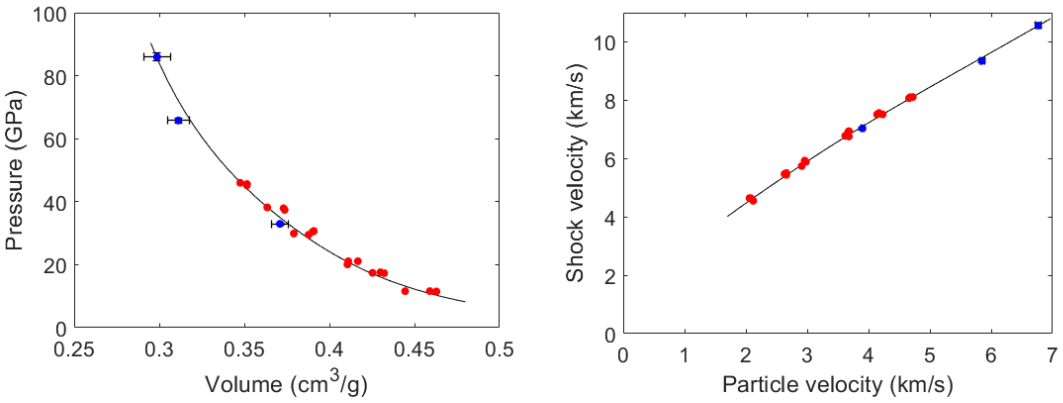

(a) Shock pressure as function of specific volume.

(b) Shock velocity as function of mass velocity.

Figure C.1. Liquid oxygen shock Hugoniot. The calculated values are shown as black lines, compared to experimental data from [30] (red) and [44] (blue).

C.2. Hydrogen

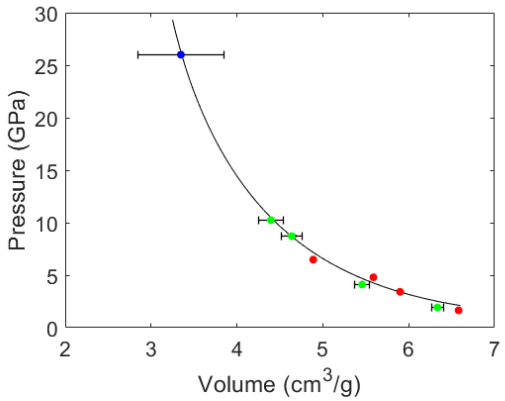

(a) Shock pressure as function of specific volume.

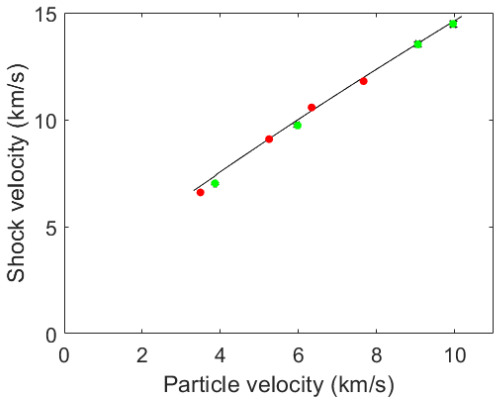

(b) Shock velocity as function of mass velocity.

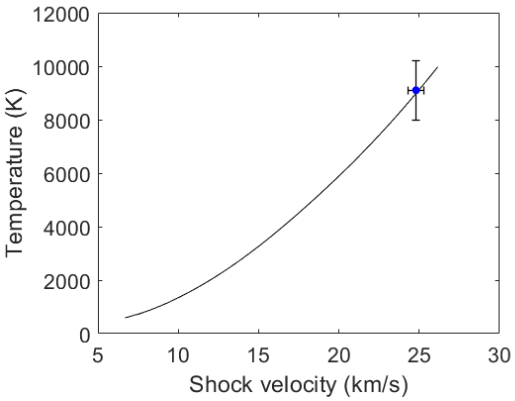

(c) Temperature as function of shock velocity.

Figure C.2. Liquid hydrogen shock Hugoniot. The calculated values are shown as black lines, compared to experimental data from [30] (red), [55] (green) and [56] (blue).

C.3. Carbon dioxide

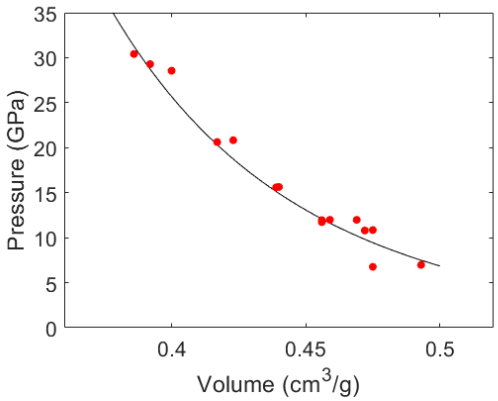

(a) Shock pressure as function of specific volume.

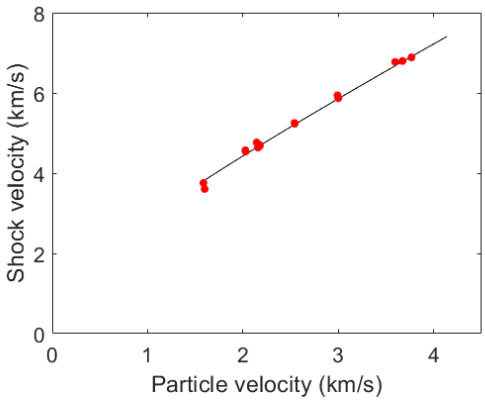

(b) Shock velocity as function of mass velocity.

Figure C.3. Liquid carbon dioxide shock Hugoniot. The calculated values are shown as black lines, compared to experimental data from [57] (red dots).

C.4. Ammonia

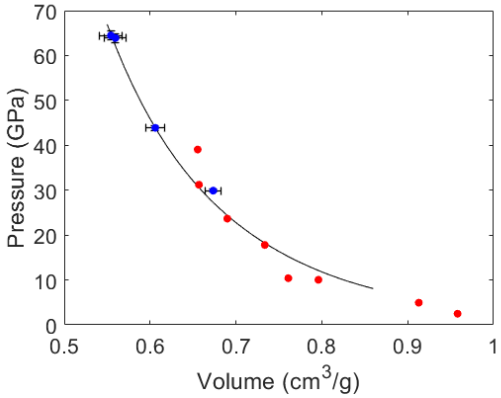

(a) Shock pressure as function of specific volume.

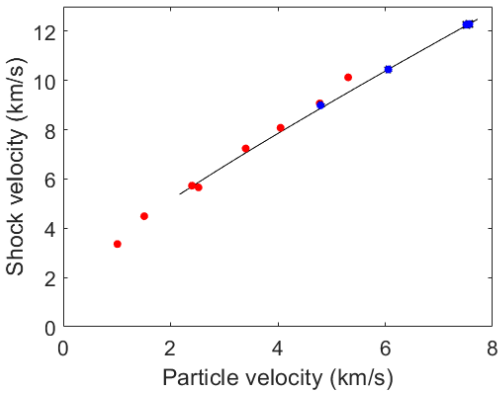

(b) Shock velocity as function of mass velocity.

Figure C.4. Liquid ammonia shock Hugoniot. The calculated values are shown as black lines, compared to experimental data from [30] (red) and [45] (blue).